

A Parallel, 2-DOF Exoskeleton for the Human Shoulder: Device Characterization and Preliminary Results on Healthy Subjects

Rainier Natividad (✉ rfnatividad@u.nus.edu)

National University of Singapore Faculty of Engineering <https://orcid.org/0000-0002-7143-1874>

Tiana Miller-Jackson

National University of Singapore

Chen-Hua, Raye Yeow

National University of Singapore

Research

Keywords: Fabric Actuators, Shoulder Exosuit, Shoulder Exoskeleton, Soft Exoskeleton, Pneumatic Bending Actuator, Soft Robotic Actuator, Wearable Robot, Muscle Activation

Posted Date: May 26th, 2020

DOI: <https://doi.org/10.21203/rs.3.rs-30545/v1>

License:  This work is licensed under a Creative Commons Attribution 4.0 International License.

[Read Full License](#)

A Parallel, 2-DOF Exoskeleton for the Human Shoulder: Device Characterization and Preliminary Results on Healthy Subjects

1 **Rainier F. Natividad**^{1,2}, **Tiana Miller-Jackson**^{1,2}, **Raye Yeow Chen-Hua**^{1,2,3*}

2 ¹Evolution Innovation Lab, Department of Biomedical Engineering, National University of
3 Singapore (NUS), Singapore

4 ²Advanced Robotics Centre (ARC), National University of Singapore (NUS), Singapore

5 ³Singapore Institute of Neurotechnology (SINAPSE), National University of Singapore (NUS),
6 Singapore

7

8 *** Correspondence:**

9 Raye Yeow Chen-Hua

10 bieych@nus.edu.sg

11 **Keywords: Fabric Actuators, Shoulder Exosuit, Shoulder Exoskeleton, Soft Exoskeleton,**
12 **Pneumatic Bending Actuator, Soft Robotic Actuator, Wearable Robot, Muscle Activation.**

13

14 **1 Abstract**

15 **1.1 Background**

16 Humans are highly reliant on the efficient function of their upper limb. Neuromuscular disorders that
17 impair the function of the shoulder consequently reduce quality of life. Robotic rehabilitation serves
18 as an attractive treatment choice due to its promising results and its ability to alleviate the demands on

19 therapists and clinicians. Nevertheless, current robotic architectures are not optimized for the human
20 shoulder but are more apt for industrial environments. Pneumatically powered soft robotic actuators
21 present an attractive method to create shoulder exoskeletons due to their compliance and relatively low
22 mass. However, current actuators lack the necessary functions to provide support to the entire
23 shoulder's range of motion.

24 **1.2 Methods**

25 A modular, fabric pneumatic actuator was constructed. The actuator design allows it to perform three-
26 dimensional (3-D) bends with minimal resistance. Four actuators were combined to create a soft
27 shoulder exoskeleton. Each actuator drives one direction of motion: elevation and depression, rotation
28 of the plane of elevation. The torque output of the actuator was measured using a customized two-axis
29 torque measurement system. Exoskeleton functionality was tested through surface electromyography
30 of relevant shoulder muscles. 10 healthy subjects were recruited and performed arm motions under the
31 assistance of the exoskeleton.

32 **1.3 Results**

33 The actuator can reach full bending ($>360^\circ$) with low pressures ($\sim 10\text{kPa}$). Its torque output is highly
34 dependent on its geometry. Moreover, torque output is reduced as the bending angles increase. The
35 actuators installed on the exoskeleton output $11.15\text{N}\cdot\text{m}$ of torque at the neutral position, and $4.44\text{N}\cdot\text{m}$
36 at 90° shoulder elevation. The test on healthy subjects showed that use of the exoskeleton reduces
37 muscle activation by up to 65% when performing shoulder elevation, and up to 34% when rotating the
38 plane of elevation. Use of the exoskeleton also resulted in a change in arm trajectory when performing
39 elevation and depression movements.

40 **1.4 Conclusions**

41 The reduction in muscle activation highlights the ability of a soft-robotic exoskeleton in supporting
42 arm movements. Moreover, the presented exoskeleton design successfully demonstrated its ability to
43 generate two degree-of-freedom support for the human shoulder

44 **2 Background**

45 The human arm is responsible for a majority of movements necessary for activities of daily living
46 (ADL) (1). As a result, humans are extremely reliant on their arms in order to live an optimal life. The
47 shoulder acts as the base of the human arm and grants the arm with maximum mobility due to the
48 shoulders nearly spherical range of motion. It is imperative to restore proper mobility to the shoulder
49 when its function is impaired (2). Clinical upper-limb exoskeletons are used as an adjunct to treat
50 disorders that inhibit shoulder movement (3,4). Typically, these exoskeletons are constructed using
51 techniques pioneered in industrial robotics. Rigid electric motors are placed concentrically with the
52 humeral head while rigid links are attached parallel to the humerus, connecting the motors to the arm.

53 The shoulder joint, also known as the shoulder complex, is typically oversimplified as a ball-and-socket
54 joint (5,6). In reality, the shoulder complex is a system of multiple joints: the scapulothoracic joint,
55 the sternoclavicular joint, the acromioclavicular joint, and the glenohumeral (GH) joint. These joints
56 connect the sternum, clavicle, scapula and humerus to form the shoulder complex. The four joints move
57 in concert, constantly translating the location of the humeral head during shoulder motion (7). This
58 motion is called scapulohumeral rhythm. Robotic shoulder exoskeletons must therefore account for the
59 unique movement of the shoulder complex (8), typically by translating the position of the motors during
60 shoulder movement (5). Alternatively, designers also employ an additional link in order to account for
61 translation of the humeral head. However, the addition of such a link increases the likelihood of joint
62 misalignment (9). Moreover, these designs weigh substantially heavier relative to the weight of a
63 human, which adds unwanted inertia to the arm and restricts the mobility of the user.

64 In contrast to traditional robotic designs, soft robotics utilizes naturally flexible materials, both as prime
65 movers and structural links. This archetype of robotics behaves similar to continuum structures (10) as
66 compared to a system of rigid bodies that typically characterize traditional robots. The distinct
67 compliance and usage of non-rigid power transmission elements have enabled soft robots to more
68 closely emulate the movement of animals. They are uniquely suited to power robotic exoskeletons due
69 to their compliance, which results in the ability to conform to the external structure of the human body,
70 and accurately follow the movement of the shoulder complex. Soft robots can be created in various
71 forms, with each form having its own method of power transmission, such as cable-driven devices
72 (11,12), shape-memory actuators (13), combustion (14), magnetism (15), and pressurized fluids (16).
73 Cable-driven actuators (17) most closely mimic the structure of the muscular system but require
74 accurate positioning of anchor points.

75 Another form of power transmission for soft robotics, pressurized fluids and specifically compressed
76 air, have proven to be a popular choice for driving clinical exoskeletons(18–22) . However, most fluidic
77 actuators are unable to provide sufficient mobility for the shoulder. Simpson et al constructed an
78 exosuit that provides abduction support. The suit is primarily actuated by a reinforced inflatable bladder
79 placed on the armpit (23) We also constructed a similar device by placing an inflatable bladder on the
80 superior side of the humerus. Inflating the bladder increases its stiffness and generates abduction
81 support for the user (24). O’Neill et al constructed an exosuit capable of providing support for
82 abduction, and horizontal flexion and extension. While their exoskeleton also possesses two-degrees
83 of freedom (DOF), it is unclear if it is capable of performing reaching actions (e.g. forward flexion),
84 which is essential in performing a variety of ADLs (25). Moreover, evidence regarding the efficacy of
85 pneumatic shoulder exoskeletons is scarce. To the extent of the authors’ knowledge, testing data on
86 humans has only involved a limited number of subjects (23,27). An expanded test on a greater number
87 of human subjects would provide a more conclusive picture on the effectiveness of these exoskeletons

88 in performing rehabilitative tasks. Moreover, it can also aid future research towards the implementation
89 of additional features into pneumatic exoskeletons.

90 This study presents a soft robotic, pneumatic, shoulder exoskeleton with 2-DOF (**Figure 1**). The
91 exoskeleton is capable of performing forward flexion and extension, abduction and adduction, and
92 horizontal flexion and extension. It can likewise drive the upper arm to any pose in between these
93 standard positions. At the core of the exoskeleton are four modular, pneumatic bending actuators with
94 separated and replaceable inflation modules. Two antagonistic actuator pairs are placed along the
95 length of the humerus. One side of each pair is responsible for one direction of motion while the agonist
96 drives the humerus in the opposite direction. The exoskeleton is unique in that the synchronized and
97 simultaneous operation of the antagonistic pairs, coupled with the additional flexibility offered by
98 separated modules, allows for multi-directional movement of the exoskeleton.

99 A detailed description of the design of the actuator and exoskeleton are presented. Changes in the
100 actuator's pose and output blocked torque as a function of input pressure and actuator bending angle
101 were measured. We previously presented a hybrid plastic-fabric actuator with replaceable inflation
102 modules (24). The present study introduces a superior fabric actuator that possesses the key
103 characteristics of the hybrid actuator while eliminating its most restrictive limitations. The reduction
104 in the internal mechanical resistance of the actuator and the reduced volumetric footprint brought about
105 in the new design allow an actuator pair to create three-dimensional (3-D) bends. Finally, an
106 experiment was conducted on ten healthy subjects in order to ascertain the exoskeleton's effects on the
107 shoulder's muscle activation and trajectory. In the subsequent sections, shoulder positions follow the
108 globe coordinate system (26) while a separate system is used to describe the actuator. The coordinate
109 system of the actuator enables a more intuitive understanding of its mechanics. The neutral position of
110 the arm coincides with the -180° position of the actuator, while an arm elevation of 90° coincides with
111 the actuator's -90° position.

112 3 Methods

113 3.1 Actuator Design

114 The primary purpose of the actuators is to provide a combination of torques to the upper arm such that
115 the exoskeleton can push the arm to any point on the anatomical workspace in one single motion. In
116 order to do so, the actuators must be able to combine their operation in that operation of multiple
117 actuator pairs can generate diagonal motion of the humerus. Moreover, any shoulder exoskeleton,
118 whether hard or soft, must not cause a significant increase in inertia and its motors' or actuators' centers
119 of rotation must always coincide with that of the humeral head in order to avoid injury. In order to
120 address these functional requirements, the actuator used in the present study is composed of a fabric
121 spine and fabric inflation modules (**Figure 2-A**). The use of pneumatics reduces the mass of the
122 actuators as compared to hydraulics. Flexible 3-D printed structures are placed on the spine and
123 modules to serve as mating and locking mechanisms. The fabrication steps are detailed in **additional**
124 **file 1**. The actuator is activated through the injection of compressed air, with a maximum continuous
125 applied pressure limited to 80kPa in order to minimize safety risks. The resulting spatial interference
126 between adjacent, inflated modules generates a bending moment that causes the actuator to generate
127 torque. The torque generated by pneumatic actuators is directly related to their size (27,28). Module
128 sizing was restricted to ensure a moderate exoskeleton size that is wearable.

129 The actuator is assembled by combining appropriate modules of varying lengths and widths based on
130 mechanical requirements (**Figure 2-B**). A long groove is placed on the 3D-printed spine structure,
131 which mates with corresponding beams on the module structure. This pair acts as a guide so that the
132 two components are properly placed. Slots are placed on the spine structure which subsequently mate
133 with studs on the module. The studs snap into place and lock the module into position (**Figure 2-C**).
134 A strip of industrial-grade hook fastener is placed on the spine, which is then subsequently attached to

135 a neoprene sheet (i.e. exoskeleton base). The modules are then secured into place, and pneumatic lines
136 are plugged into each module using polyethylene (PET) connectors. The pneumatic lines start from a
137 pressure regulator or valve and branch out to the individual modules. Fabric straps are placed along the
138 center of the modules in order to prevent unnecessary inflation along the covered area (**Figure 2-B**).
139 Without the straps, the middle section (i.e. section covered by the straps) will inflate but will not
140 contribute in the generation of torque and will decrease actuation speed (29). In its neutral, deflated
141 state, the adjacent modules fold up on the sides. The actuators behave as continuum structures when
142 pressurized. The folded-up modules inflate and spatially interfere with adjacent modules. When
143 unloaded and unattached to external structures, the actuator curls into a smooth spiral shape until each
144 module is in point contact with its adjacent module (**Figure 2-D**). The separated structure of the
145 inflation modules, the flexibility of the fabric spine, and the absence of side seams grants
146 unprecedented 3-D flexibility to the actuator. **Figure 2-E** shows an inflated actuator in a helical pose.
147 The helical shape is only achievable through the actuators' flexibility. This enables the actuator to
148 perform tight 3-D bends while still maintaining its torque output in its active axis of rotation. This
149 ability to perform 3-D bends allows the actuators to combine their directions of motions while the
150 modular feature of the actuators allows it to reposition its midpoint so that the exoskeleton may be
151 adjusted to each user.

152 **3.2 Actuator Principle of Operation**

153 In order to fully understand the principle of operation of the actuator, a physical model was created.
154 The actuator generates force, and subsequently torque, through the spatial interference between
155 adjacent modules. There are n modules installed in each actuator, with $n/2+1$ intersecting pairs of
156 modules. Each j^{th} pair consists of the i^{th} and $i+1$ modules. Each module pair generates its own force
157 (\vec{F}_j), depending on the nature of the intersection of the modules, as well as their interaction with the
158 environment, and subsequently contributes to the overall torque produced by the actuator. This means

159 that an actuator's torque output will differ depending on the topology of the object to which it is
 160 attached. This model simulates an actuator's attachment to the human shoulder and assumes that the
 161 actuator is bent at the center, while the remaining modules remain straight. In their inflated state, the
 162 modules can effectively be considered as an extruded ellipse (**Figure 3-A, Figure 3-B**) with the lengths
 163 of the minor and major axes to be equal to half of the module's inflated height (H_i) and length (L_i).

164 **Figure 3-C** shows the free-body diagrams upon which the rest of the model is based. In this
 165 configuration, the actuator effectively generates torque with respect to the pivot point; it can be
 166 effectively divided into two equal segments, with each segment generating equal but opposing torques
 167 that effectively bring the entire system into static equilibrium. Each segment is further subdivided into
 168 three sections: the angled section (middle pair, red), the edge section (first and last pair, yellow), and
 169 the straight middle section (all other pairs, blue). Each section will have its own unique mechanical
 170 behaviors; the subsequent subsections will concentrate on the $n/2+1$ to the n th module. The total torque
 171 (T_{Total}) generated by the actuator is the sum of each module's generated torque (T_i) [1].

$$172 \quad T_{Total} = \sum_{i=1}^{n/2} T_i \quad [1]$$

173

174 **3.2.1 Force from module intersections (\vec{F}_j)**

175 \vec{F}_j is dependent on the nature of the contact area (A_c) between two colliding modules. Due to the
 176 elliptical shape of the modules, this model approximates the contact area as a rectangle. The contact
 177 area can be determined by examining the cross-section as seen from the top-view (**Figure 3-D**). The
 178 centers, $C_i = (C_{i,x}, C_{i,y})$ and $C_{i+1} = (C_{i+1,x}, C_{i+1,y})$ of the two ellipses are first established; in the proceeding
 179 calculations, both centers lie on the x-axis while the origin coincides with C_{i+1} . Points $M_i = (M_{i,x}, M_{i,y})$
 180 and $M_{i+1} = (M_{i+1,x}, M_{i+1,y})$ are the points of attachment on the fabric spine. Upon inflation, modules

181 collide and rotationally displace by the bending angle (θ_j). They then trace a circular path centered
 182 around point O_j ; the arc length of this path is equal to module spacing (d). $C_{i,x}$ can then be calculated:

$$183 \quad C_{ix} = H_i \sin \frac{\theta}{2} + \frac{2d}{\theta} \sin \frac{\theta}{2} + H_{i+1} \sin \frac{\theta}{2} \quad [2]$$

$$184 \quad C_{ix} = (H_i + H_{i+1} + \frac{2d}{\theta}) \sin \frac{\theta}{2} \quad [3]$$

185
 186 With the location of the centers known, the ellipses can now be mathematically defined with [4] and
 187 [5]
 188

$$189 \quad \mathbf{1} = \left(\frac{(x_i - C_{ix}) \left(\cos \frac{\theta}{2} \right) + (y_i - C_{iy}) \left(\sin \frac{\theta}{2} \right)}{\frac{H_i}{2}} \right)^2 + \left(\frac{(y_i - C_{iy}) \left(\cos \frac{\theta}{2} \right) - (x_i - C_{ix}) \left(\sin \frac{\theta}{2} \right)}{\frac{L_i}{2}} \right)^2 \quad [4]$$

$$190$$

$$191 \quad \mathbf{1} = \left(\frac{(x_{i+1} - C_{i+1x}) \left(\cos \frac{\theta}{2} \right) + (y_{i+1} - C_{i+1y}) \left(\sin \frac{\theta}{2} \right)}{\frac{H_{i+1}}{2}} \right)^2 + \left(\frac{(y_{i+1} - C_{i+1y}) \left(\cos \frac{\theta}{2} \right) - (x_{i+1} - C_{i+1x}) \left(\sin \frac{\theta}{2} \right)}{\frac{L_{i+1}}{2}} \right)^2$$

$$192 \quad [5]$$

193 The points of intersection, $I_{j,1} = (I_{j,1,x}, I_{j,1,y})$ and $I_{j,2} = (I_{j,2,x}, I_{j,2,y})$, between the two ellipses are
 194 determined by simultaneously solving [4] and [5]. The quadratic nature of expressions [4] and [5] can
 195 produce up to four points in intersection. To prevent the model from underestimating the size of the
 196 contact area, the two points with the largest linear distance between them are chosen. The rectangular
 197 area A_c is then calculated using [6], where W_i is the module's width. The line of action of the force
 198 vector (\vec{F}_j) is assumed to lie within the center of and is normal to A_c ; \vec{F}_j is calculated through [7], where
 199 P is the pressure inside the modules.

201
$$A_C = d(I_{j,1}, I_{j,2})(W_i) \quad [6]$$

202
$$\vec{F}_j = (PA_C) \cdot \frac{I_{j,1} \times I_{j,2}}{\|I_{j,1} \times I_{j,2}\|} \text{ where } \vec{F}_j = (F_{j,x}, F_{j,y}) \quad [7]$$

203
204 **3.2.2 The angled section ($\frac{n}{2} + 1$ and $\frac{n}{2} - 1$ module)**

205 The angled section transmits a vertical force and a horizontal force to the arm or body which is
206 subsequently converted to torque. The vertical force is effectively transmitted as a linear distributed
207 load, while the horizontal force can be effectively considered as a point load. This horizontal force is
208 also opposed by the contact in the $j/2+1$ pair; it is important to note that the modules of the $j/2+1$ pair
209 are oriented 0° from each other (i.e. $\theta=0^\circ$). The torque generated by the angled section ($T_{\frac{n}{2}+1}$) is
210 given by [8].

211
$$T_{\frac{n}{2}+1} = H_{\frac{n}{2}} \mathbf{x} \left(\vec{F}_{\frac{n}{4}} - \vec{F}_{\frac{n}{4}+1} \right) + \frac{d(M_{\frac{n}{2}+1} - I_{\frac{n}{4}+1})}{3} \mathbf{x} \left(\vec{F}_{\frac{n}{4}} \right) \quad [8]$$

212 At $\theta > -90^\circ$, the vertical component of \vec{F}_j ($F_{j,y}$) no longer contributes to torque generation due to the
213 fact that vertical force is now directed away from the arm, and is transformed into tension on the
214 fabric spine, as opposed to generating a counter-acting force on the arm. This results in minor
215 compression of the actuator but does not significantly affect its performance. At $\theta > -90^\circ$, $T_{\frac{n}{2}+1}$ is
216 described by [9].

217
$$T_{\frac{n}{2}+1} = H_{\frac{n}{2}+1} \mathbf{x} \left(\vec{F}_{\frac{n}{4}} - \vec{F}_{\frac{n}{4}+1} \right) \quad [9]$$

218 **3.2.3 The middle section (all other modules)**

219 It can be seen in **Figure 3-C** that each module along the middle sections generates equal and opposing
 220 forces from their intersection with their neighboring modules. This results in zero torque generation
 221 for modules in the middle section.

223

222
$$T_i = H_i \chi(\vec{F}_j - \vec{F}_{j+1}) = 0 \text{ where } n \neq 1, n, \frac{n}{2} + 1, \frac{n}{2} - 1 \text{ and } j \neq \frac{n}{2}, \frac{n}{4}, \frac{n}{4} - 1 \text{ [10]}$$

224 **3.2.4 The edge section (1st and nth module)**

225 It is assumed that the modules adjacent to the edge module (i.e. 2nd and n-1 module) are oriented
 226 parallel to the edge module (i.e. $\theta=0^\circ$). Therefore, only a single force generates torque for the
 227 module. The torque generated by the edge section (T_n) is given by [11]

228
$$T_n = H_n \chi\left(\vec{F}_{\frac{n}{2}}\right) \text{ [11]}$$

229

230 Finally, (1) can be expanded into (12)

231
$$T_{Total} = \begin{cases} H_{\frac{n}{2}+1} \chi\left(\vec{F}_{\frac{n}{4}} - \vec{F}_{\frac{n}{4}+1}\right) + \frac{d(M_{\frac{n}{2}+1} - I_{\frac{n}{4}})}{3} \chi\left(\vec{F}_{\frac{n}{4}}\right) + H_n \chi\left(\vec{F}_{\frac{n}{2}}\right), & \theta_{\frac{n}{4}} \leq -90 \\ H_{\frac{n}{2}+1} \chi\left(\vec{F}_{\frac{n}{4}} - \vec{F}_{\frac{n}{4}+1}\right) + H_n \chi\left(\vec{F}_{\frac{n}{2}}\right), & \theta_{\frac{n}{4}} > -90 \end{cases} \text{ [12]}$$

232 **3.3 The 2-DOF Exoskeleton**

233 The base of the exoskeleton is a customized neoprene sleeve that acts as a platform to which the spines
 234 can be attached. The neoprene sleeve features straps along the torso to ensure that it remains secure
 235 during operation. Four actuators, configured as two antagonistic pairs, are placed on the shoulder, with

236 each actuator positioned 90° from each other (**Figure 1**). Each pair is responsible for each degree of
237 freedom—one pair performs humerus elevation and depression, while another performs rotation of the
238 humerus' plane of elevation. The depression actuator starts from the base of the neck, tracing the
239 superior side of the humerus. The elevation actuator is placed on the inferior side, starting from the
240 lateral area of the ribcage and extending through the armpit and the arm. The steering actuators are
241 placed on the anterior and posterior arm starting from the sternum and the spine, respectively.
242 Additional modules, positioned as to have minimum possible contact area, are added along the upper
243 arm. These modules have minute overlap and are essentially in point contact when pressurized. They
244 act as a means to distribute the load generated by the bending actuators throughout the entire upper
245 arm. These modules slightly bend and effectively act as straight beams. Such a seamless system could
246 easily be extended to other joints in the arm, such as the elbow and the wrist. However, a system for
247 the entire arm is beyond the scope of this paper. The exoskeleton is controlled by a pneumatic control
248 system; exoskeleton output is controlled by regulating the pressure supplied to the actuators. The
249 details of the control system are available in **additional file 1**.

250 The operation of the actuators allows the humerus to trace a natural trajectory. From the neutral
251 position, the humerus can perform shoulder abduction and adduction by activating the elevation or
252 depression actuators (**Figure 4-A**). The shoulder can also be rotated along the plane of elevation by
253 sequentially activating the elevation and steering actuators (**Figure 4-B**). Simultaneous activation of
254 the elevation and steering actuators also grants the ability to perform shoulder flexion or extension
255 (**Figure 4-C**). A video of these movements is made available to supplement this paper (**Additional file**
256 **2**). In addition to performing the basic anatomical movements, the controlled activation of both steering
257 actuators and the elevation actuators allows the performance of reaching actions (**Figure 4-D, Figure**
258 **4-E**).

259 **3.4 Actuator Experiments**

260 In order to verify the accuracy of the physical model, three actuator variants were constructed, with
 261 each variant having a total of eight modules installed. The variants differ in the size and pattern of the
 262 modules installed. Their geometric parameters are listed in **Table 1**. Module widths were based on the
 263 lower 5th percentile of female upper arm diameters for B, and the lower 5th percentile of male upper
 264 arm diameters for C (27). Module spacing (d) was set at 25mm in order to minimize the discontinuity
 265 in the curvature profile of the actuator. While tighter spacing is desired, the size of the 3-D printed
 266 locking structures presents a practical minimum. Alternate module patterning (i.e. ABAB, ACAC) was
 267 chosen since a homogenous pattern induced buckling in preliminary tests. This pattern involves the
 268 installation of alternating module sizes; specifically, module A was installed between each B and C
 269 module. The module lengths were then set to 65mm and 90mm to ensure sufficient spatial interference
 270 between adjacent modules.

271 The actuator' static free bending output in response to a pressure input was measured by hanging the
 272 actuator vertically. The detailed setup is available in **additional file 1**.

TABLE 1. MODULE DIMENSIONS AND PATTERNING

Module Variants	<i>Module Length (L)</i>	<i>Module Width (W)</i>
A	65mm	55mm
B	90mm	55mm
C	90mm	65mm
Actuator Variant	Module Patterning^a	
D1	AAAAAAAA	
D2	ABABABAB	
D3	ACACACAC	

a. The installation arrangement of modules on the variants

273 A two-axis torque measurement system was used to measure the actuators' static performance (**Figure**
274 **5-A**). As an inflatable structure, an inflated actuator will always attempt to remain in a 2-D pose by
275 generating a straightening torque when acted upon by an external force that drives it into a 3-D pose.
276 While the actuator is only capable of generating torque along its primary axis, it is important to quantify
277 how much unwanted straightening torque the actuators generate when forced into a 3-D pose. As shown
278 in **Figure 5-B and Figure 5-C**, the A-A' axis coincides with the actuator's primary axis of bending,
279 while the B-B' axis is perpendicular to A-A' axis. The A-A' angle corresponds to θ in the physical
280 model. A fully folded actuator corresponds to an A-A' angle of -180° while 0° is straight. A detailed
281 explanation of the measurement system is available in **additional file 1**.

282 All experiments were repeated three times, and the samples were dismounted and remounted before
283 each repetition in order to minimize the effects of any actuator movement that may have occurred
284 during a measurement.

285 **3.5 Healthy Subject Testing Protocol**

286 Ten healthy subjects were recruited into the study; the test was reviewed and approved by NUS
287 Institutional Review Board (N-17-103). Willing subjects who had no history of injuries relating to the
288 upper limb and possess body mass index (BMI) between the range of 18.5 to 24.9 were allowed to
289 participate. A summarized list of the recruited subjects' anthropomorphic measurements related to the
290 upper arm is available in **Additional File 1**. Subjects were only required to attend a single session.
291 Informed consent was acquired at the start of the session and anthropomorphic measurements were
292 recorded.

293 The exoskeleton was adapted to the subject at the start of the test by changing the modules attached.
294 Actuator variant D2 was attached and the number and spacing of non-bending modules were adjusted
295 until the length of the actuators reached the elbow. After acquiring consent, surface electromyography

296 (sEMG) sensors (Delsys, Trigno Wireless) were attached to the lateral, anterior and posterior deltoid,
297 the clavicular head of the pectoralis major and the infraspinatus relating to the right arm. The test
298 focused on the right arm of the subject in order to circumvent electrocardiograph (ECG) contamination
299 of the sEMG signals. Meanwhile, an inertial measurement unit, or IMU, (Bosch, BN055) was attached
300 to the chest, lying on the sternum and oriented parallel to the transverse plane; another IMU was
301 attached to the medial right, upper arm. While motion capture technology is typically used for such
302 tests [118], [133]–[136], this technique relies on the application of passive motion markers on the limb
303 that are tracked by optical cameras. The nature of the exoskeleton prohibits the utilization of motion
304 capture due to the fact that the inflatable modules have the tendency to block the line of sight of the
305 camera to the markers. The IMUs are positioned in a manner wherein they are in identical orientations
306 when the arm is abducted to 90°. **Figure 6** shows the application of the sEMG and IMU sensors. The
307 sEMGs and IMUs were sampled at 2000Hz and 100Hz respectively. To facilitate IMU mapping during
308 data processing, subjects were instructed to position their arm into three standard anatomical positions:
309 the neutral position, 90° shoulder abduction, and 90° forward flexion (**Figure 6-D**). IMU readings were
310 then recorded as the arms were kept stationary at these positions. Warm-up exercises were performed
311 for approximately five minutes. At this stage, the subjects were also asked to familiarize themselves
312 with the associated movements involved in the test. Maximum voluntary contraction (MVC) of the
313 muscles was recorded next. Subjects were asked to place their limbs in the neutral position; a researcher
314 then held the arm stationary while the subject attempted to perform shoulder abduction; a similar action
315 activity was performed for shoulder flexion. From the 90° abduction position, subjects performed
316 horizontal shoulder flexion.

317 Three arm motions were investigated: shoulder abduction and adduction, shoulder flexion and
318 extension, and shoulder horizontal flexion and extension. Movements were performed until the arm
319 reached a minimum of 90° of the target movement, and the reverse motion was subsequently

320 performed. Each movement was repeated three times. Each type of motion was conducted under
321 different speeds – fast and slow. The slow speed corresponds to an angular velocity of 30°/s while fast
322 movements corresponded to an angular velocity of 90°/s. These values correspond to the average
323 execution speed of ADLs involving the human shoulder (30). Subjects guided themselves during
324 movements. At the peak of each movement, the subject was instructed to pause in order to ensure that
325 each movement was isolated from the proceeding movement. Once the sensors were applied, the
326 subjects donned a neoprene sleeve to ensure that the sEMG sensors remain stationary and to minimize
327 the presence of motion artifacts.

328 The test was conducted in three phases. The first phase (free phase, F) serves as a baseline; the subjects
329 were asked to perform arm motions while only wearing an empty neoprene sleeve (**Figure 6-E**). In the
330 second phase (unpowered phase ,U), the neoprene sleeve was removed, and the subjects wore an
331 unpowered exoskeleton (**Figure 6-F**). At this stage, the exoskeleton was disconnected from the control
332 system. Subjects continued to perform arm motions under their own power. This phase is designed to
333 measure the mechanical resistance of the exoskeleton in terms of the amount of muscular effort
334 necessary to move the arm and the exoskeleton. Finally, the exoskeleton was powered in the third phase
335 (powered phase, P). During the powered phase of horizontal flexion and extension, subjects elevated
336 their arm under their own power.

337 Data sets were segmented based on the condition (i.e. free, unpowered, or powered), and movement
338 direction. Comparisons were performed by calculating the root mean square (RMS) of the IMU
339 trajectory data and normalized muscle activation data for each segment. Overall, three comparison
340 types were made based on their conditions: powered against free (PvF), powered against unpowered
341 (PvU), and unpowered against free (UvF). The data processing techniques are detailed in **Additional**
342 **File 1**.

343 4 Results

344 4.1 Actuator Static Characteristics

345 Each actuator, when unloaded, was able to achieve full bending ($>360^\circ$) when excited with a pressure
346 of 10kPa. An increase in pressure did not have any effect on its pose.

347 **Figure 7-A** shows the results of each variant's torque output, as a function of A-A' angle, at 30°
348 increments. The measurements were acquired by setting the B-B' angle to 0° and pressurizing the
349 actuator to 80kPa. Meanwhile, **Figure 7-B** shows the torque output of the actuator as a function of the
350 input pressure. These measurements were taken at an A-A' angle of -90° and a B-B' angle of 0° . The
351 pressure inside the actuators was varied from 0kPa to 80kPa. It can be seen that the static physical
352 model is able to accurately follow the behavior of the actuators as observed by the experiments. When
353 predicting the relationship between torque and angle, as seen in **Figure 7-A**, the model had mean errors
354 of 21.7%, 20.9%, and 15.8% for D1, D2 and D3 variants, respectively. The model exhibited mean
355 errors of 16.2%, 28.3% and 14.9% when predicting torque verses pressure response (**Figure 7-B**).
356 Overall, both the data and the model suggest that the actuator exhibits an exponential decrease in torque
357 output as the A-A angle is increased. The actuators are able to apply maximum torque from A-A' angle
358 -180° to -90° , with variants D1, D2 and D3 exhibiting peak torques of 10.24 N-m, 11.15 N-m and
359 15.54 N-m, respectively. Meanwhile, they exhibit torques of 1.27 N-m, 4.44 N-m, and 4.66 N-m at -
360 90° , the angle at which the arm imposes maximum static load on the actuator (-90° A-A' angle
361 corresponds to 90° of shoulder elevation). The actuator's torque output effectively becomes constant
362 at A-A' angle 0° to 90° . They exhibited torques of 0.84 N-m, 1.54 N-m, and 1.80N-m at on this range.
363 The unfolding nature of the modules ensure that the contact area is nearly constant when the actuator
364 is positioned between 0° to 90° . They also suggest that torque output has a linear response to increases
365 in pressure.

366 An increased reduction in available contact area occurs when the A-A' angle and B-B' angle change
367 simultaneously. The effects of this behavior on variant D2 are shown in **Figure 7-C**. In this
368 measurement, the A-A' angle was set to -90° and the B-B' angle was varied from 45° to 0° at 15°
369 increments. This range of motion corresponds to that required of the majority of ADLs (19). The
370 actuator was then pressurized to 80kPa. An overall decrease in the torque output along the A-A' axis
371 was found as the B-B' angle was increased. However, the platform was not able to detect any
372 significant torque output ($>0.5\text{N}\cdot\text{m}$) along the B-B' axis. This can be attributed to the ability of each
373 individual module to translate in 3-D as well as the aspect ratio of the modules; they show minimal
374 surface area along the B-B' axis. Effectively, the modules reposition themselves such that there is
375 minimal resistance during operation, resulting in small B-B' torques.

376 **4.2 Arm Trajectory**

377 Trajectories extracted from a single subject are shown in **Figure 8**. Each subject was able to reach the
378 90° arm position for all motions as observed during the test. Application of the exoskeleton increased
379 the starting angle of elevation from 0° (i.e. neutral position/pendulum position) to $\sim 15^\circ$. However, it is
380 interesting to note that each subject was able to return to true neutral position (i.e. 0°) after the first
381 cycle. This is attributed to the forced movement of the subject, allowing each subject to overcome the
382 resistance introduced by the exoskeleton and forcibly return to true neutral. A closer visual inspection
383 of the individual trajectories shows an observable difference in the paths among the three phases.

384 The full tabular data of the change in RMS of the arm trajectories are found in **Additional file 1 (Table**
385 **S2 and Table S3)**. Fast, arm elevation movements (i.e. fast abduction and fast forward flexion) show
386 a definite change in arm trajectory in PvF comparisons. However, the change in trajectory across
387 subjects is not consistent, with most results being statistically insignificant (i.e. $p>0.05$) in PvF and
388 PvU comparisons. No statistically significant results were observed for UvF comparisons which can

389 suggest that the mechanical structure itself does not cause this change in trajectory. Instead, the change
390 in the behavior of arm movements is attributed to the dissimilar movement of the actuator and the arm,
391 and not due to the mechanical resistance introduced by the exoskeleton. It's also interesting to note
392 that the exoskeleton does not affect horizontal flexion and extension; while there was an 8% change in
393 the trajectory PvU horizontal extension, this change is minimal.

394 **4.3 Muscular Activation**

395 **Figure 8** also features the time-series muscle activation — shown as EMG voltage readings normalized
396 to MVC — of a single subject across various movements and phases. Visual analysis indicates a
397 correlation between muscle activation and arm position: muscle activation increases as arm is flexed
398 or abducted and respectively decreases as it is extended or adducted. These results are expected given
399 that the mechanical load on the muscles increases as the arm is positioned away from the neutral
400 position. Among the same the movement and muscles, the shapes of the activation graphs show similar
401 patterns and structure. However, there is an apparent offset between the plots from different phases
402 suggesting a change in the overall magnitude of muscle activation between the free, unpowered, and
403 powered phases. **Figure 9** and **figure 10** show the summarized relative change in muscle activation for
404 relevant muscles for slow and fast movements respectively. Numerical versions of these results are
405 provided in **Additional file 1 (Table S4 and Table S5)**.

406 The results show a decrease in the mean RMS of muscle activation in the population for fast PvF
407 comparisons. Statistically significant results were obtained from multiple muscles during fast
408 exercises: the lateral deltoid and infraspinatus during abduction and adduction, the anterior deltoid
409 during forward flexion and extension, the pectoralis major during horizontal flexion, and the pectoralis
410 major and posterior deltoid during horizontal extension. The exoskeleton was able to reduce deltoid
411 activation by 65% ($p < 0.01$) when performing abduction and adduction, and by 45% ($p < 0.01$) and 25%

412 ($p < 0.05$) when performing forward flexion and extension, respectively. The activation of the pectoralis
413 major was reduced by 34% ($p < 0.05$) when rotating the arm's angle of plane of elevation. While
414 reductions in some muscles were also observed during slow movements, the reduction magnitude was
415 considerably lower as compared to those acquired during fast movements. Statistically significant
416 results were only obtained for the anterior deltoid and lateral deltoid during slow forward flexion and
417 extension, and the anterior deltoid for horizontal extension. The slow movements only apply minimal
418 loads to the shoulder muscles that result in low magnitudes in the measured EMG voltages, which
419 explains the high variance in non-significant findings. The assistance provided by the exoskeleton
420 would not be apparent in the voltage waveform due to the inherent, relatively low signal-to-noise ratio
421 of EMG (31). Nevertheless, the statistically significant results for forward flexion and extension
422 indicate that the exoskeleton is capable of providing support during reaching movements.

423 Similar to PvF comparisons, PvU comparisons showed reductions in muscle activations. Statistically
424 significant results were obtained during fast movements for all relevant muscles in abduction and
425 adduction, horizontal flexion and extension, and the anterior deltoid for forward flexion and extension.
426 These particular muscles exhibited similar results in PvF comparisons. Meanwhile slow movements
427 yielded more statistically significant values in contrast to PvF. All muscles relating to abduction and
428 adduction, the pectoralis major during horizontal flexion and extension, and the lateral deltoid during
429 forward flexion and extension also achieved statistical significance.

430 Meanwhile, the results for UvF comparisons vary for both speeds. Pectoralis major activation increased
431 by 29% ($p < 0.05$) while performing fast horizontal flexion and extension. Lateral deltoid activation
432 increased by 25% ($p > 0.05$) and 28% ($p > 0.05$) while performing slow abduction and adduction,
433 respectively, while infraspinatus activation increased by 10% ($p > 0.05$) when performing slow
434 abduction and adduction. Other muscles did not feature statistically significant readings. Most notably,
435 forward flexion and extension did not exhibit any change in muscle activation for both speeds. The

436 high variance in the data is attributed to the various strategies employed by the subjects in order to defy
437 the mechanical resistance added by the exoskeleton, with some strategies more successful than others.
438 Moreover, the fit of the sleeve to a participant may also play a role in the amount of mechanical
439 resistance it would impart on the user.

440 **5 Discussion**

441 The ultimate goal of this paper is to create an effective and elegant solution to the current mechanical
442 and kinematic complexities surrounding the design of robotic shoulder exoskeletons for clinical
443 rehabilitation. To avoid the complexities involved in using traditional robotic architectures, we
444 employed a fabric-based, pneumatic soft actuator to drive a shoulder exoskeleton. The actuator was
445 developed based on the hybrid fabric-plastic design and results we previously presented (27,28). The
446 majority of the actuator is composed of nylon fabric, which resulted in negligible bending resistance
447 as evidenced by its ability to trace its full range of motion with minimal input. This feature, along with
448 its soft robotic nature, ensured that the shoulder sleeve will have maximum mechanical transparency.
449 Results from various tests indicate that the exoskeleton will be able to provide torque assistance
450 regardless of the position of the actuators or the pressure supplied. Nevertheless, the positions of the
451 actuators influence their torque outputs. Load bearing actuators must operate from the -180° to -90° A-
452 A' angle range in order to maximize their utility. This behavior is consistent with that from our previous
453 work(27,28). These actuators would supply approximately 7%, 24.6% and 25.8% of the torque
454 necessary to maintain arm elevation of 90° for a typical, stretched, male arm with a mass of 3.5kg (32).
455 Users can still benefit from the high peak torques at low elevation angles (i.e. -180° to -90° A-A') when
456 performing high velocity, dynamic movements.

457 The final design of the exoskeleton is intended to capitalize on the capabilities of the modular actuators.
458 When comparing the torque curves of the D2 and D3 variants, it can be seen that the difference is

459 negligible. This suggests that minor buckling occurs with the D3 actuator and that a significant portion
460 of the energy injected in the D3 variant is transformed into unwanted curling of the actuator between
461 modules, which results in extremely diminished torque output. While this amount of buckling will not
462 pose a safety risk, the D3 variant is not suitable for use in an exoskeleton. Using hook-and-loop
463 fasteners, the actuators can be specifically placed on the body of each user. The use of neoprene as the
464 primary material for the sleeve provided the exoskeleton with an elastic base that tightly follows the
465 contours of the body. This allows the sleeve and the actuators to remain in the correct position. The
466 positioning of the actuators takes advantage of their torque-angle curve. Using this configuration, the
467 majority of the loads are to be handled by the elevation actuator. This actuator primarily operates in
468 the -180° to -90° A-A' region, which is the region of maximum torque. The steering actuators reside
469 in the 0° to 90° A-A' region, where the torque-angle relationship is effectively constant. Moreover, the
470 actuators are mounted in a parallel configuration. This allows the exoskeleton to distribute its force
471 application throughout the entire surface area of the arm. The use of antagonistic actuators also negates
472 the effect of drift during deflation since the agonist will be primarily responsible for deflating the
473 actuator. An additional feature of the modular spine is that the torque output of both pairs can be
474 combined such that they can trace trajectories outside a single actuator's axis of rotation. This can be
475 achieved through the simultaneous activation of both pairs.

476 A proper evaluation of the exoskeleton, along with the actuators, involves testing on a human shoulder
477 in order to quantify their benefits and drawbacks as well as providing insight on potential design
478 improvements that otherwise may not become apparent. The test performed for this paper examined
479 the ability of the exoskeleton to assist upper arm movement through the quantitative measurements of
480 relevant muscle activations. The comparison of powered and unpowered movements conclusively
481 demonstrated lessened muscle activation when assisted by the powered exoskeleton, which
482 consequently indicates that the exoskeleton effectively provides torque to the human arm. Likewise,

483 the comparison of powered movements and free movements show the exoskeleton's capability to
484 reduce muscle activation. It can reduce deltoid activation by up to 65% while performing abduction
485 and adduction, and is also capable of providing multi-DOF support, which allows subjects to perform
486 forward flexion and extension. While the exoskeleton also reduced muscle activation by 45% during
487 forward flexion movements, the amount of assistance was reduced to 25% when performing the
488 equivalent unloading motion (i.e. forward extension). This is due to the reduced overall load on the
489 muscles when performing extension movements as compared to performing flexion movements.
490 Furthermore, the exoskeleton was able to steer the arm's angle of plane of elevation, which reduced
491 muscle activation by 33% when performing horizontal flexion and extension. This amount of mobility
492 is attributed to the unique actuator design. While the actuator can only actively generate torque in one
493 axis, the separated module design allows it to perform 3-D movements when acted upon by an external
494 force (i.e. a secondary actuator mounted perpendicularly). A traditional, planar, pneumatic bending
495 actuator would generate resistive torque, forcing it to return to a 2-D, planar shape, and reduce its
496 effectiveness in providing 2-DOF support.

497 The use of fabric components allowed for the construction of a powered exoskeleton that imparts
498 minimal mechanical resistance to the human arm. The fabric actuators allow for a simple exoskeleton
499 design that accurately follows the movement of the humeral head without the need for simplistic
500 biomechanical approximations or overly-complicated alignment compensation mechanisms typically
501 employed in traditional, shoulder exoskeletons(33). No unintended loading on other muscles were
502 detected during all of the tests. UvF comparisons yielded statistically significant data for horizontal
503 flexion and extension, and slow abduction and adduction, which indicate that the mechanical structure
504 of the exoskeleton increases muscle activation. While the exoskeleton may have increased the
505 mechanical resistance in other areas of the arm, this amount of resistance is presumably relatively
506 insignificant in relation to the gravity load of the arm itself and was even undetectable through sEMG.

507 The mean RMS values show that activation of shoulder muscles during fast unpowered movements
508 increased by up to 29%, as compared to free movements, and slow movements showed an increase of
509 up to 48%. However, it must be noted that the absolute change in activation is negligible since the
510 overall load on the arm is similarly smaller during slow movements. Nevertheless, both PvF and PvU
511 comparisons yielded the same amount of muscle activation reduction, indicating that the exoskeleton
512 is not only capable of overcoming its own mechanical resistance, but also capable of effectively
513 negating it.

514 The unique soft structure of the exoskeleton also allowed subjects to retain their shoulder's natural
515 range of motion regardless of the prevailing condition (i.e. free, unpowered or powered phase). While
516 their relaxed, neutral position was elevated by approximately 15° when wearing the exoskeleton, each
517 subject was still able to reach the true neutral position (i.e. 0° elevation) when effort was applied. While
518 this required the application of force on the arm—either by the user, or the exoskeleton—the results
519 show that the exoskeleton was able to compensate, and overall muscular activation was still reduced.
520 Meanwhile, the statistical results for fast forward flexion and extension, fast abduction, and slow
521 abduction seem to suggest that use of the exoskeleton affects elevation movements. These nevertheless
522 indicate that the use of the exoskeleton, in its current form, will reduce the kinematic accuracy of the
523 user's arm. It is important to note that subjects were only given one day to use the exoskeleton, and
524 further training and familiarization may allow them to regain movement accuracy (34).

525 The results highlight the positive benefits of the exoskeleton to the user by measuring sEMG signals
526 as way to ascertain its effects on muscle activation. A comprehensive comparison of the results of the
527 exoskeleton with that found in the literature is currently not possible due to a lack of a standard
528 evaluation protocol. By using an unsuited state as a baseline, we were able to remove the mechanical
529 resistance imparted by the actuators from our measurements. This is not always the case when
530 exoskeletons are evaluated. Nevertheless, sEMG measurements have also been used to assess

531 exoskeleton performance. O'Neill et al was able to achieve 62.75% of muscle reduction on the lateral
532 deltoid when performing abduction and 16.94% on the pectoralis major when performing horizontal
533 flexion (35). Simpson et al also collected sEMG signals, but their data processing method was different
534 from the one presented here (23). Tiseni et al achieved a mean reduction of 56.9% on the lateral deltoid
535 using a hybrid soft-hard exoskeleton on five healthy subjects (36). The vast other majority of functional
536 tests with exoskeletons directly deal with subjects with shoulder impairments. They typically
537 implement clinical tests which are designed to gauge the level of shoulder functionality.

538 It is important to note that the exoskeleton lacks a controller that involves human input in the activation
539 of the exoskeleton's functions. Admittance control has proven to be effective in predicting the onset of
540 user motion and has been implemented in a number of exoskeletons (37,38). Continuum-based
541 actuators impart forces on a large surface area, making it impractical to measure forces through
542 conventional sensors. While the addition of an admittance controller would improve the performance
543 of the exoskeleton, it is difficult to implement. We believe that the observed changes in arm trajectory
544 when wearing the powered exoskeleton is also a product of a lack of user input in the control system.
545 The inclusion of intent sensing would allow the exoskeleton to make on-the-fly adjustments to its
546 motion and will therefore reduce its effect on the user's kinematics. These changes are therefore a
547 product of the lack of synchronization between the user and the exoskeleton, and not of the mechanical
548 design of the exoskeleton. The build quality of the exoskeleton in the current study also limited possible
549 performance. The exoskeleton was only capable of withstanding 80kPa of continuous, sustained
550 pressure and 150kPa of intermittent pressure. Improving the build quality delays, the onset of device
551 failure, which could lead to the ability to handle higher intermittent pressures and the generation of
552 stronger torques. While there is evidence of mechanical resistance throughout the exoskeleton's range
553 of motion, the resistance of the steering actuators must be significantly reduced. Natural, free, shoulder
554 movement in this direction only presents minimal load to the shoulder muscles and the exoskeleton

555 should therefore present the relatively same amount of low resistance. Reduced mechanical resistance
556 would also simplify the application of an admittance-based controller for backdrivability.

557 **6 Conclusion**

558 The exoskeleton presented demonstrated the feasibility of creating a fabric-based shoulder
559 exoskeleton, powered by flexible pneumatic actuators. The torque response and free bending response
560 of the underlying actuator were explored. The exoskeleton was tested on healthy subjects in order to
561 measure its efficacy. Our results quantitatively demonstrated the efficacy of our exoskeleton in
562 imparting torque to the shoulder joint. While there are limitations to our study, the results suggest that
563 the unique exoskeleton configuration is effective in providing support to the human shoulder
564 throughout its entire range of motion. We were able to create an exoskeleton configuration with two
565 degrees-of-freedom. It is able to support not only abduction and adduction, and horizontal flexion and
566 extension, but also reaching motions (i.e. forward flexion and extension). Reaching movements allow
567 the exoskeleton to assist the users in a wide variety of ADLs in a seamless manner. While these ADLs
568 may possibly be accomplished using sequential humeral elevation and rotation of the plane of
569 elevation, this series of motions is undoubtedly unnatural. Moreover, the exoskeleton was able to
570 provide support throughout the entire range of motion of the shoulder and this mainly attributed to the
571 minimal mechanical resistance of the actuator coupled with the parallel actuation configuration of the
572 exoskeleton.

573 **7 List of Abbreviations and Symbols**

FULL MEANING	ABBREVIATION
Three-Dimensional	3-D
Activities of Daily Living	ADL
Glenohumeral	GH

Degrees-of-Freedom	DOF
Polyethylene	PET
Body Mass Index	BMI
Actuator Active Axis of Bending	A-A'
Actuator Passive Axis of Bending	B-B'
Electrocardiography	ECG
Surface Electromyography	sEMG
Inertial Measurement Unit	IMU
Maximum Voluntary Contraction	MVC
Root Mean Square	RMS
Powered against Free Comparison	PvF
Powered against Unpowered Comparison	PvU
Unpowered against Free Comparison	UvF

Mathematical Interpretation	Symbol
Force Generated by A Module Pair	\vec{F}_j
Module Inflated Height	H_i
Module Inflated Length	L_i
Torque Generated by A Segment or Actuator	T_x
Contact Area of a Module Pair	A_c
Module Centroid	C_i
Module Mounting Coordinate	M_i
Module Bending Angle. Equivalent To A-A' Angle	Θ_j
Center Of Rotation of a Module Pair	O_j
Point of Intersection Between Adjacent Modules	$I_{j,n}$
Applied Pressure	P

576 The human subject test was approved by the National University of Singapore Institutional Review
577 Board (N-17-103).

578 **9 Consent for Publication**

579 The subjects' informed consent was acquired in accordance with NUSB-IRB guidelines. Subjects
580 also consented to the publication of collected data.

581 **10 Availability of data and materials**

582 The datasets used and/or analysed during the current study are available from the corresponding
583 author on reasonable request.

584 **11 Competing Interests**

585 The authors declare that the research was conducted in the absence of any commercial or financial
586 relationships that could be construed as a potential conflict of interest.

587 **12 Author Contributions**

588 RF and RY conceptualized the project. RF manufactured the devices. RF and TMJ performed the
589 experiments. RF analyzed the results. RY provided technical guidance for the project. All authors
590 helped in editing the manuscript.

591 **13 Funding**

592 Research supported by MOE AcRF Tier 2 (R-397-000-281-112)

593 **14 Acknowledgements**

594 Ms. Marie Angela Ordonez for helping prepare the manuscript.

595 **15 References**

- 596 1. Magermans DJ, Chadwick EKJ, Veeger HEJ, Van Der Helm FCT. Requirements for upper
597 extremity motions during activities of daily living. *Clin Biomech.* 2005;20(6):591–9.
- 598 2. Terry GC, Chopp TM. Functional Anatomy of the Shoulder. *J Athl Train.* 2000;35(3):248–55.
- 599 3. Norouzi-Gheidari N, Archambault PS, Fung J. Effects of robot-assisted therapy on stroke
600 rehabilitation in upper limbs: Systematic review and meta-analysis of the literature. *J Rehabil*
601 *Res Dev.* 2012;49(4):479–96.
- 602 4. Lum PPS, Burgar CCG, Shor PC, Majmundar M, Van der Loos M, Gresham G, et al. Robot-
603 Assisted Movement Training Compared With Conventional Therapy Techniques for the
604 Rehabilitation of Upper-Limb Motor Function After Stroke Peter. 2002 Jul [cited 2016 Sep
605 6];83(7). Available from: <http://www.ncbi.nlm.nih.gov/pubmed/12098155>
- 606 5. Nef T, Guidali M, Riener R. ARMin III - arm therapy exoskeleton with an ergonomic shoulder
607 actuation. *Appl Bionics Biomech.* 2009;6(2):127–42.
- 608 6. Schiele A, Van Der Helm FCT. Kinematic design to improve ergonomics in human machine
609 interaction. *IEEE Trans Neural Syst Rehabil Eng.* 2006;14(4):456–69.
- 610 7. Ludewig PM, Phadke V, Braman JP, Hassett DR, Cieminski CJ, Laprade RF. Motion of the
611 shoulder complex during multiplanar humeral elevation. Vol. 91, *Journal of Bone and Joint*
612 *Surgery - Series A.* 2009. p. 378–89.
- 613 8. Niyetkaliyev AS, Hussain S, Ghayesh MH, Alici G. Review on Design and Control Aspects of
614 Robotic Shoulder Rehabilitation Orthoses. *IEEE Transactions on Human-Machine Systems*
615 [Internet]. 2017 [cited 2017 Jun 13];1–12. Available from:
616 <http://ieeexplore.ieee.org/document/7932920/>
- 617 9. Carignan C, Liszka M, Roderick S. Design of an arm exoskeleton with scapula motion for
618 shoulder rehabilitation. In: 2005 International Conference on Advanced Robotics, ICAR '05,
619 Proceedings [Internet]. Seattle, WA: IEEE; 2005. p. 524–31. Available from:
620 <https://ieeexplore.ieee.org/document/1507459>
- 621 10. Mosadegh B, Polygerinos P, Keplinger C, Wennstedt S, Shepherd RF, Gupta U, et al.
622 Pneumatic Networks for Soft Robotics that Actuate Rapidly. *Adv Funct Mater* [Internet]. 2014
623 Apr 10 [cited 2016 Jun 21];24(15):2163–70. Available from:
624 <http://doi.wiley.com/10.1002/adfm.201303288>
- 625 11. Manti M, Hassan T, Passetti G, D'Elia N, Laschi C, Cianchetti M. A Bioinspired Soft Robotic
626 Gripper for Adaptable and Effective Grasping. *Soft Robot* [Internet]. 2015 Sep [cited 2017 Jul
627 25];2(3):107–16. Available from: <http://online.liebertpub.com/doi/10.1089/soro.2015.0009>
- 628 12. Xiloyannis M, Cappello L, Binh KD, Antuvan CW, Masia L. Preliminary design and control
629 of a soft exosuit for assisting elbow movements and hand grasping in activities of daily living.
630 *J Rehabil Assist Technol Eng.* 2017;4:205566831668031.

- 631 13. Seok S, Onal CD, Cho K-J, Wood RJ, Rus D, Kim S. Meshworm: A Peristaltic Soft Robot
632 With Antagonistic Nickel Titanium Coil Actuators. *IEEE/ASME Trans Mechatronics*. 2013
633 Oct;18(5):1485–97.
- 634 14. Loepfe M, Schumacher CM, Lustenberger UB, Stark WJ. An Untethered , Jumping Roly-Poly
635 Soft Robot Driven by Combustion. 2015;2(1):33–42.
- 636 15. Alouges F, DeSimone A, Giraldi L, Zoppello M. Can Magnetic Multilayers Propel Artificial
637 Microswimmers Mimicking Sperm Cells? *Soft Robot*. 2015;2(3):117–28.
- 638 16. Shepherd RF, Ilievski F, Choi W, Morin SA, Stokes AA, Mazzeo AD, et al. Multigait soft
639 robot. *Proc Natl Acad Sci [Internet]*. 2011;108(51):20400–3. Available from:
640 <http://www.pnas.org/cgi/doi/10.1073/pnas.1116564108>
- 641 17. Galiana I, Hammond FL, Howe RD, Popovic MB. Wearable soft robotic device for post-
642 stroke shoulder rehabilitation: Identifying misalignments. In: 2012 IEEE/RSJ International
643 Conference on Intelligent Robots and Systems [Internet]. IEEE; 2012. p. 317–22. Available
644 from: <http://ieeexplore.ieee.org/document/6385786/>
- 645 18. Yap HK, Khin PM, Koh TH, Sun Y, Liang X, Lim JH, et al. A Fully Fabric-Based
646 Bidirectional Soft Robotic Glove for Assistance and Rehabilitation of Hand Impaired Patients.
647 *IEEE Robot Autom Lett*. 2017;2(3):1383–90.
- 648 19. Stilli A, Cremoni A, Bianchi M, Ridolfi A, Gerii F, Vannetti F, et al. AirExGlove-A novel
649 pneumatic exoskeleton glove for adaptive hand rehabilitation in post-stroke patients. 2018
650 *IEEE Int Conf Soft Robot RoboSoft 2018*. 2018;579–84.
- 651 20. Fang J, Yuan J, Wang M, Xiao L, Yang J, Lin Z, et al. Novel Accordion-Inspired Foldable
652 Pneumatic Actuators for Knee Assistive Devices. *Soft Robot*. 2019;00(00):1–14.
- 653 21. Ezzibdeh R, Arora P, Amanatullah DF. Utilization of a pneumatic exoskeleton after total knee
654 arthroplasty. *Arthroplast Today [Internet]*. 2019;8–9. Available from:
655 <https://doi.org/10.1016/j.artd.2019.02.008>
- 656 22. Sanchez RJ, Wolbrecht E, Smith R, Liu J, Rao S, Cramer S, et al. A pneumatic robot for re-
657 training arm movement after stroke: Rationale and mechanical design. Vol. 2005, Proceedings
658 of the 2005 IEEE 9th International Conference on Rehabilitation Robotics. 2005. p. 500–4.
- 659 23. Simpson CS, Okamura AM, Hawkes EW. Exomuscle: An inflatable device for shoulder
660 abduction support. In: Proceedings - IEEE International Conference on Robotics and
661 Automation [Internet]. IEEE; 2017 [cited 2017 Aug 25]. p. 6651–7. Available from:
662 <http://ieeexplore.ieee.org/document/7989785/>
- 663 24. Natividad RF, Yeow CH. Development of a soft robotic shoulder assistive device for shoulder
664 abduction. In: 2016 6th IEEE International Conference on Biomedical Robotics and
665 Biomechatronics (BioRob) [Internet]. IEEE; 2016 [cited 2017 Sep 4]. p. 989–93. Available
666 from: <http://ieeexplore.ieee.org/document/7523758/>
- 667 25. Oosterwijk AM, Nieuwenhuis MK, van der Schans CP, Mouton LJ. Shoulder and elbow range
668 of motion for the performance of activities of daily living: A systematic review. *Physiother*

- 669 Theory Pract [Internet]. 2018;34(7):505–28. Available from:
670 <https://doi.org/10.1080/09593985.2017.1422206>
- 671 26. Doorenbosch CAM, Harlaar J, Veeger D (H. EJ. The globe system: An unambiguous
672 description of shoulder positions in daily life movements. *J Rehabil Res Dev* [Internet].
673 2003;40(2):149. Available from:
674 <http://www.rehab.research.va.gov/jour/03/40/2/PDF/doorenbosch.pdf>
- 675 27. Natividad RF, Del Rosario MRJ, Chen PCY, Yeow RCH. A Reconfigurable Pneumatic
676 Bending Actuator with Replaceable Inflation Modules. *Soft Robot* [Internet]. 2018;5(3):304–
677 17. Available from: <http://www.liebertpub.com/doi/10.1089/soro.2017.0064>
- 678 28. Natividad RF, Del Rosario MRJ, Chen PCY, Yeow RCH. A Hybrid Plastic-Fabric Soft
679 Bending Actuator with Reconfigurable Bending Profiles. In: *Proceedings - IEEE International*
680 *Conference on Robotics and Automation* [Internet]. Singapore: IEEE; 2017 [cited 2017 Aug
681 21]. p. 6700–5. Available from: <http://ieeexplore.ieee.org/document/7989792/>
- 682 29. Mosadegh B, Polygerinos P, Keplinger C, Wennstedt S, Shepherd RF, Gupta U, et al.
683 Pneumatic Networks for Soft Robotics that Actuate Rapidly. *Adv Funct Mater* [Internet]. 2014
684 Apr 10 [cited 2016 Jun 21];24(15):2163–70. Available from:
685 <http://doi.wiley.com/10.1002/adfm.201303288>
- 686 30. Murgia A, Hortobágyi T, Wijnen A, Bruin L, Diercks R, Dekker R. Effects of age and sex on
687 shoulder biomechanics and relative effort during functional tasks. *J Biomech* [Internet].
688 2018;81:132–9. Available from: <https://doi.org/10.1016/j.jbiomech.2018.10.001>
- 689 31. Reaz MBI, Hussain MS, Mohd-Yasin F. Techniques of EMG signal analysis: Detection,
690 processing, classification and applications. *Biol Proced Online*. 2006;8(1):11–35.
- 691 32. Plagenhoef S, Gaynor Evans F, Abdelnour T, Evans FG, Abdelnour T. Anatomical Data for
692 Analyzing Human Motion. *Res Q Exerc Sport* [Internet]. 1983;54(2):169–78. Available from:
693 <http://www.tandfonline.com/doi/abs/10.1080/02701367.1983.10605290>
- 694 33. Rehmat N, Zuo J, Meng W, Liu Q, Xie SQ, Liang H. Upper limb rehabilitation using robotic
695 exoskeleton systems: a systematic review. *Int J Intell Robot Appl* [Internet].
696 2018;(0123456789). Available from: <http://link.springer.com/10.1007/s41315-018-0064-8>
- 697 34. Kadivar Z, Beck CE, Rovekamp RN, Malley MKO, Joyce CA. On the Efficacy of Isolating
698 Shoulder and Elbow Movements with a Soft, Portable, and Wearable Robotic Device.
- 699 35. Neill CTO, Phipps NS, Cappello L, Paganoni S, Walsh CJ, O’Neill CTCT, et al. A soft
700 wearable robot for the shoulder: Design, characterization, and preliminary testing. *IEEE Int*
701 *Conf Rehabil Robot* [Internet]. 2017 Jul [cited 2017 Aug 15];02129:1672–8. Available from:
702 <http://ieeexplore.ieee.org/document/8009488/>
- 703 36. Tiseni L, Xiloyannis M, Chiaradia D, Lotti N, Solazzi M, Kooij H Van Der, et al. On the edge
704 between soft and rigid : an assistive shoulder exoskeleton with hyper-redundant kinematics.
705 2019 IEEE 16th Int Conf Rehabil Robot. 2019;618–24.
- 706 37. Xiloyannis M, Chiaradia D, Frisoli A, Masia L. Physiological and kinematic effects of a soft

707 exosuit on arm movements. *J Neuroeng Rehabil.* 2019;16(1):1–15.

708 38. Shen Y, Sun J, Ma J, Rosen J. Admittance control scheme comparison of EXO-UL8: A dual-
709 arm exoskeleton robotic system. In: *IEEE International Conference on Rehabilitation*
710 *Robotics.* 2019. p. 611–7.

711

712

713

714 **16 Figure Legends and Tables**

715 **Figure 1:**

716 Front (Left) and back (Right) views of the 2-DOF shoulder exoskeleton. The exoskeleton is powered
717 by 2 pairs of antagonistic, modular actuators. The elevation/depression pair and the steering pair are
718 attached perpendicularly.

719 **Figure 2:**

720 A) A completed spine with a completed module. The yellow and white, 3-D printed structures are
721 clearly seen on the spine and module respectively. The red band on the module indicates the location
722 of the heat-seal seam. The actuator's geometric properties are shown: [d] Module Spacing, [L]
723 Module Length, [W] Module Width. (B) The assembled actuator. The spine is attached to neoprene
724 through industrial grade hook-and-loop fasteners. Fabric straps are placed across to limit unwanted
725 inflation at the center. (C) A CAD representation of the 3-D printed structures (D) The actuator curls
726 during inflation. The strap and neoprene are removed for clarity. At this pose, all the modules are in
727 point contact with adjacent modules. (E) The actuator curls into a helix through the application of
728 external forces. Its ability to perform 3-D bending is clearly demonstrated.

729 **Figure 3**

730 (A) The actuator as represented by the physical model. The model considers the inflated modules as
731 extruded ellipses. Model segments are color coded. Red: angled section. Blue: straight middle sections.
732 Yellow: Edge sections. (B) The top view. The definition of the bending angle, θ , is shown; a straight
733 actuator corresponds to an angle of 0° . (C): The free body diagram showing how forces are applied to
734 the module and to the arm. (D) A visual representation of the mathematical expressions used to
735 determine the contact area. The modules revolve around a point O_j [green]. The line projection of the
736 rectangular contact area is shown [orange].

737 **Figure 4:**

738 The range of motion of the actuator is shown for an exoskeleton with attached D2 variants. (A)
739 Abduction or adduction. The yellow area highlights non-bending modules that lengthen the moment
740 arm of the bending modules. (B) Rotation along the plane of elevation. (C) Forward flexion or
741 extension. Alternatively, a combination of these movements can be performed through the combined
742 activation of actuators. (D-F) The exoskeleton performing reaching actions. The positions shown
743 were achieved in a single motion, starting from the neutral position.

744 **Figure 5:**

745 (A) The two-axis torque measurement system. RED: The A-A' axis. Orange: The B-B' axis. (B) A
746 top view of a schematic representation of the actuator. A straight actuator corresponds to an A-A'
747 angle of 0° while a fully folded actuator corresponds to -180° . (C) A front view of the actuator. The
748 definition of the B-B' angle is shown.

749 **Figure 6:**

750 sEMG and IMU sensors were placed on the subjects. (A) Front View. (B) Side View (C) Back View.
751 (D) Subjects were asked to perform abduction and adduction, horizontal flexion and extension, and
752 forward flexion and extension under various conditions. The (yellow) casings housing the IMUs are
753 shown. LD-Lateral Deltoid, AD-Anterior Deltoid, P-Pectoralis Major, I-Infraspinatus, PD-Posterior
754 Deltoid, Abd-Abduction, Add-Adduction, FF-Forward Flexion, FE-Forward Extension, HF-
755 Horizontal Flexion, HE-Horizontal Extension

756 **Figure 7:**

757 The experiment results for the actuator (A) Torque output as a function of A-A' angle when pressurized
758 to 80kPa. (B) Torque output at various inflation pressures, at an A-A' angle set to 90°. Solid lines
759 represent the output of the model. (C) A contour plot of torque output at various A-A' angles and B-B'
760 angles for the D2 variant. (D) The waveform in response to a 60s square wave, with 0-80kPa peak-to-
761 peak amplitudes. (E) The averaged step response during inflation. (F) The averaged step response
762 during deflation.

763 **Figure 8:**

764 Segmented trajectory and muscle activation data sets extracted from a single subject. Representative
765 muscles were chosen for visual illustration. (A) Abduction (Lateral Deltoid) and Adduction (Lateral
766 Deltoid). (B) Horizontal Flexion (Anterior Deltoid) and Horizontal Extension (Posterior Deltoid). (C)
767 Forward Flexion (Anterior Deltoid) and Forward Extension (Posterior Deltoid). Muscle activation
768 waveforms show a direct correlation with the corresponding trajectory. There is an apparent offset
769 between free, unpowered and powered phases.

770 **Figure 9:**

771 Box plots summarizing muscle activation data for slow movements. Lat Delt-Lateral Deltoid. Ant
772 Delt-Anterior Deltoids. Pos Delt-Posterior Deltoid. Pecs-Pectoralis Major. Infra-Infraspinatus

773 **Figure 10:**

774 Box plots summarizing muscle activation data for fast movements. Lat Delt-Lateral Deltoid. Ant
775 Delt-Anterior Deltoids. Pos Delt-Posterior Deltoid. Pecs-Pectoralis Major. Infra-Infraspinatus

776 **17 Additional Materials**

777 **17.1 Additional File 1**

- 778 • Format: .docx
- 779 • Title: Supplementary Information
- 780 • Description: Non-essential data and text that further enriches the reader understand the work
781 presented.

782 **17.2 Additional File 2**

- 783 • Format: .mp4
- 784 • Title: Range of Motion Demo
- 785 • Description: Video presenting capabilities of the exoskeleton

786

Figures

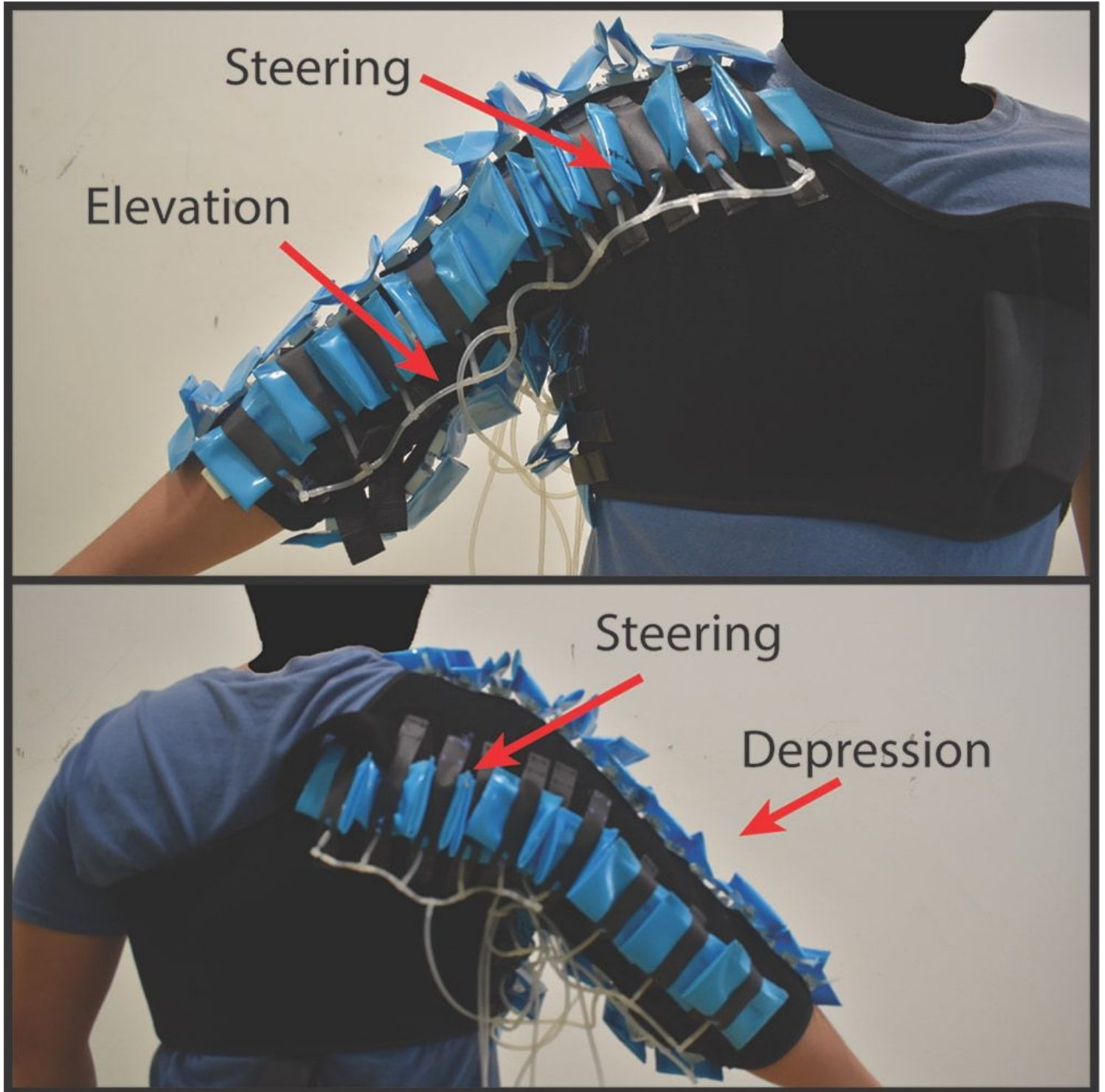


Figure 1

Front (Left) and back (Right) views of the 2-DOF shoulder exoskeleton. The exoskeleton is powered by 2 pairs of antagonistic, modular actuators. The elevation/depression pair and the steering pair are attached perpendicularly.

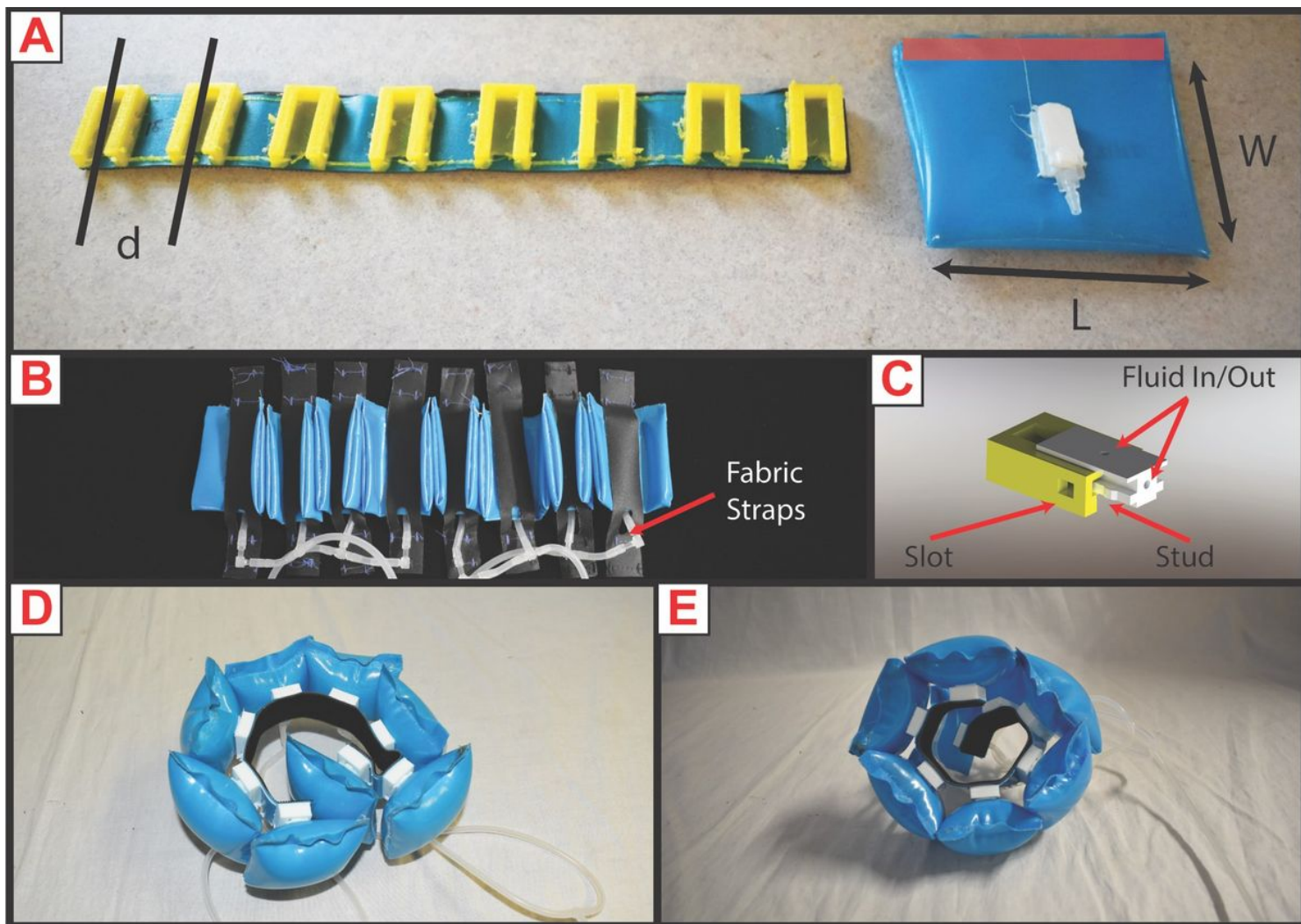


Figure 2

A) A completed spine with a completed module. The yellow and white, 3-D printed structures are clearly seen on the spine and module respectively. The red band on the module indicates the location of the heat-seal seam. The actuator's geometric properties are shown: [d] Module Spacing, [L] Module Length, [W] Module Width. (B) The assembled actuator. The spine is attached to neoprene through industrial grade hook-and-loop fasteners. Fabric straps are placed across to limit unwanted inflation at the center. (C) A CAD representation of the 3-D printed structures (D) The actuator curls during inflation. The strap and neoprene are removed for clarity. At this pose, all the modules are in point contact with adjacent modules. (E) The actuator curls into a helix through the application of external forces. Its ability to perform 3-D bending is clearly demonstrated.

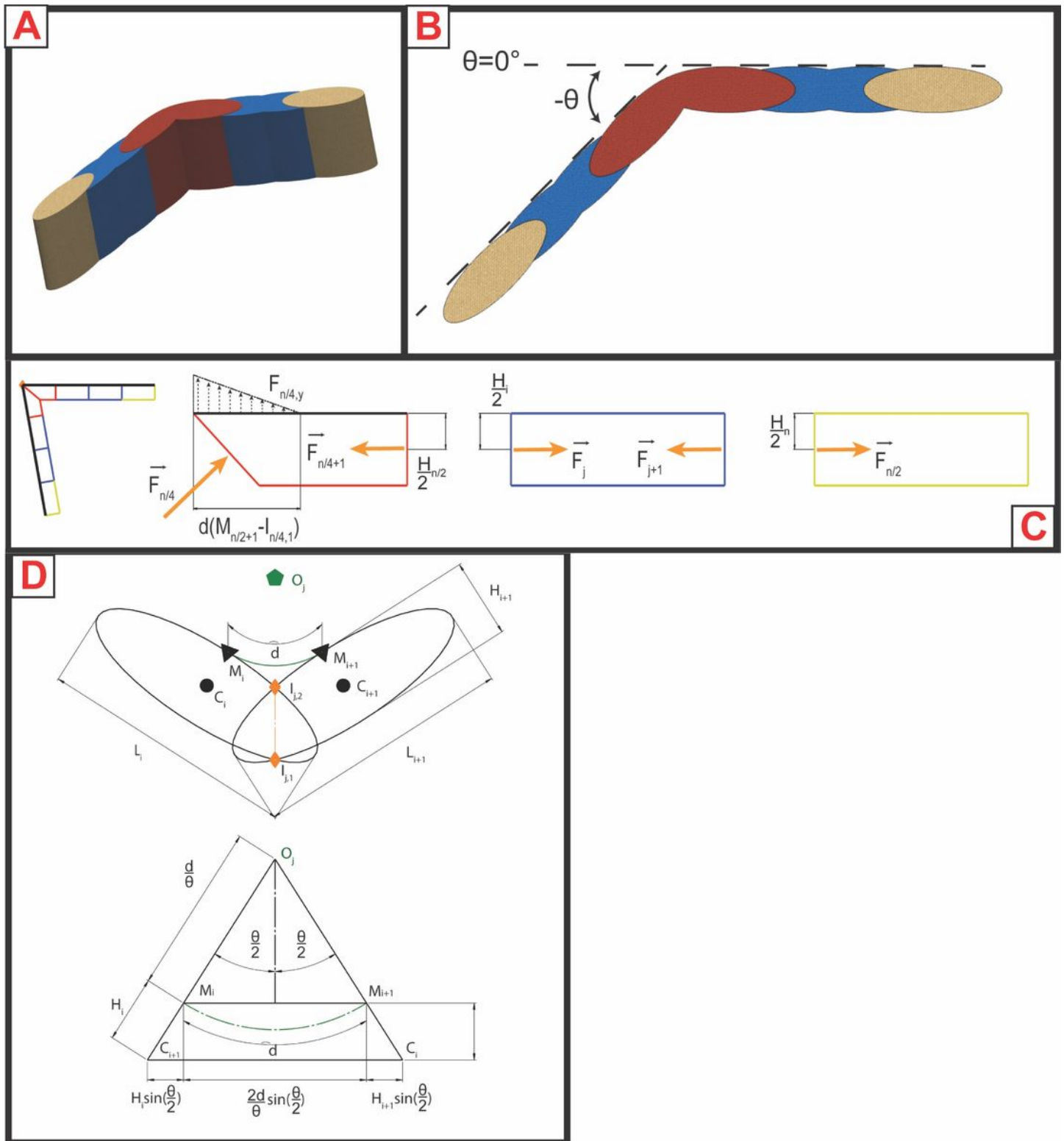


Figure 3

(A) The actuator as represented by the physical model. The model considers the inflated modules as extruded ellipses. Model segments are color coded. Red: angled section. Blue: straight middle sections. Yellow: Edge sections. (B) The top view. The definition of the bending angle, θ , is shown; a straight actuator corresponds to an angle of 0° . (C): The free body diagram showing how forces are applied to the module and to the arm. (D) A visual representation of the mathematical expressions used to determine

the contact area. The modules revolve around a point O_j [green]. The line projection of the rectangular contact area is shown [orange].

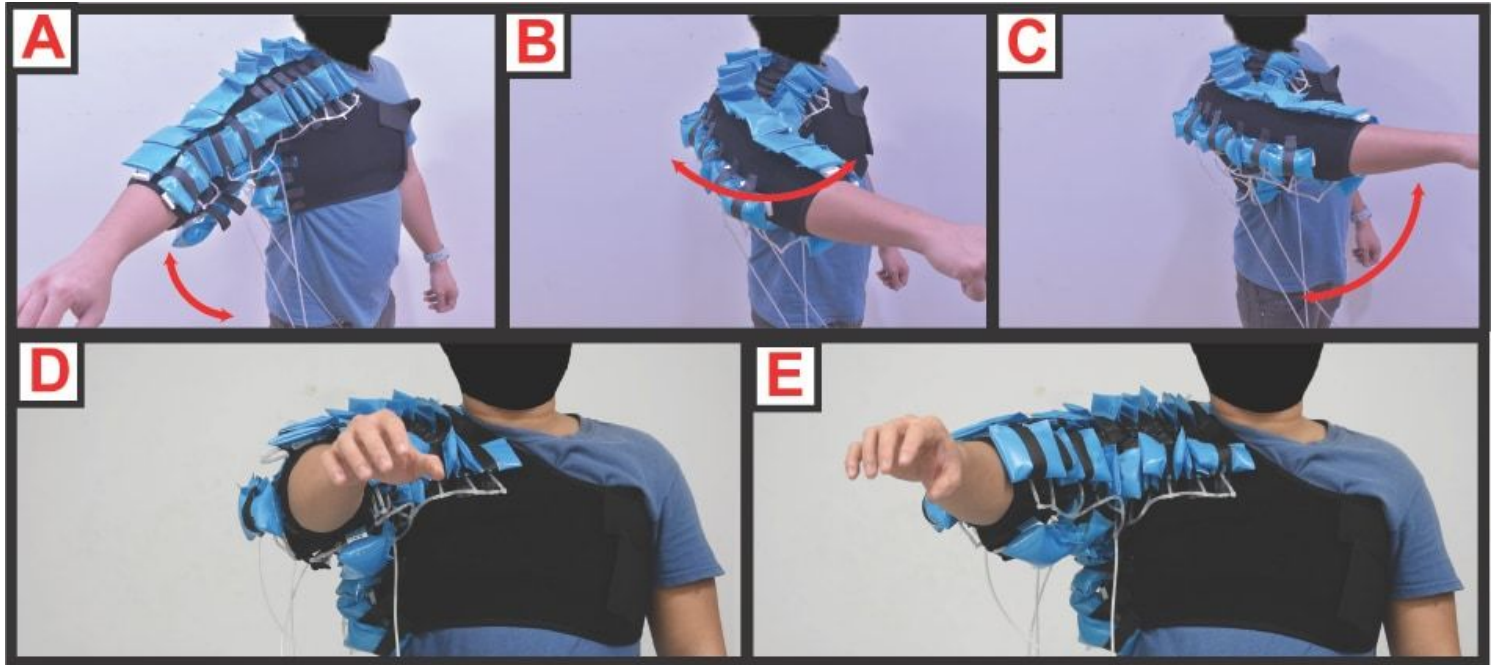


Figure 4

The range of motion of the actuator is shown for an exoskeleton with attached D2 variants. (A) Abduction or adduction. The yellow area highlights non-bending modules that lengthen the moment arm of the bending modules. (B) Rotation along the plane of elevation. (C) Forward flexion or extension. Alternatively, a combination of these movements can be performed through the combined activation of actuators. (D-F) The exoskeleton performing reaching actions. The positions shown were achieved in a single motion, starting from the neutral position.

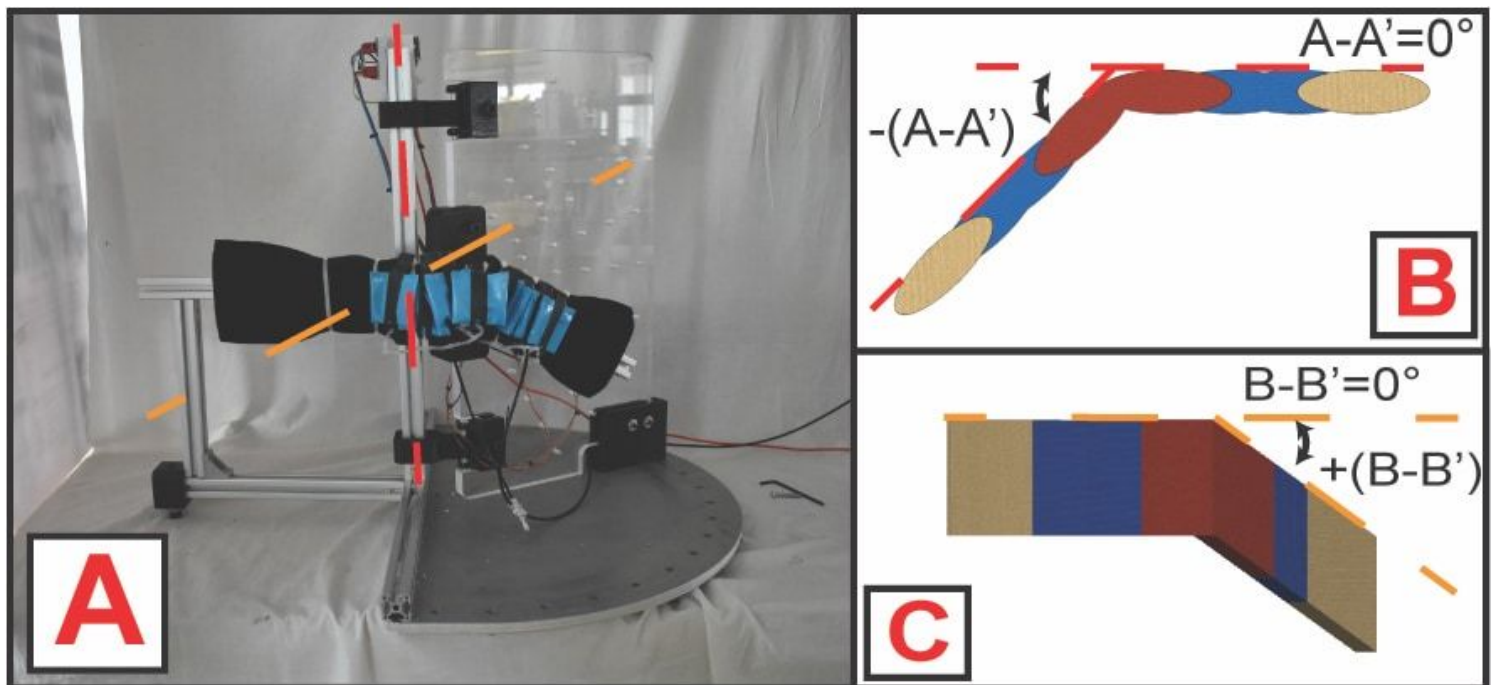


Figure 5

(A) The two-axis torque measurement system. RED: The A-A' axis. Orange: The B-B' axis. (B) A top view of a schematic representation of the actuator. A straight actuator corresponds to an A-A' angle of 0° while a fully folded actuator corresponds to -180°. (C) A front view of the actuator. The definition of the B-B' angle is shown.

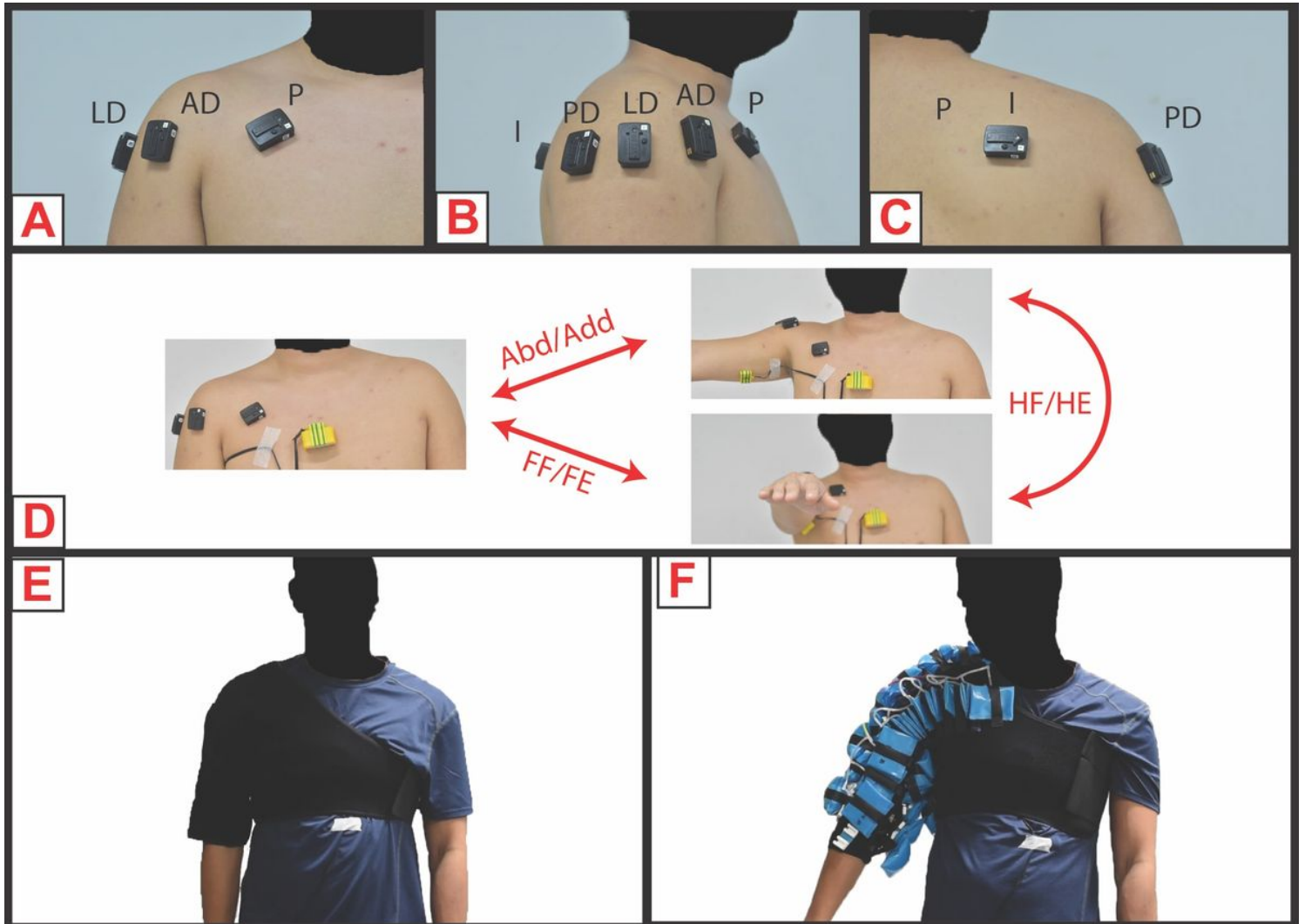


Figure 6

sEMG and IMU sensors were placed on the subjects. (A) Front View. (B) Side View (C) Back View. (D) Subjects were asked to perform abduction and adduction, horizontal flexion and extension, and forward flexion and extension under various conditions. The (yellow) casings housing the IMUs are shown. LD- Lateral Deltoid, AD-Anterior Deltoid, P-Pectoralis Major, I-Infraspinatus, PD-Posterior Deltoid, Abd- Abduction, Add-Adduction, FF-Forward Flexion, FE-Forward Extension, HF-Horizontal Flexion, HE- Horizontal Extension

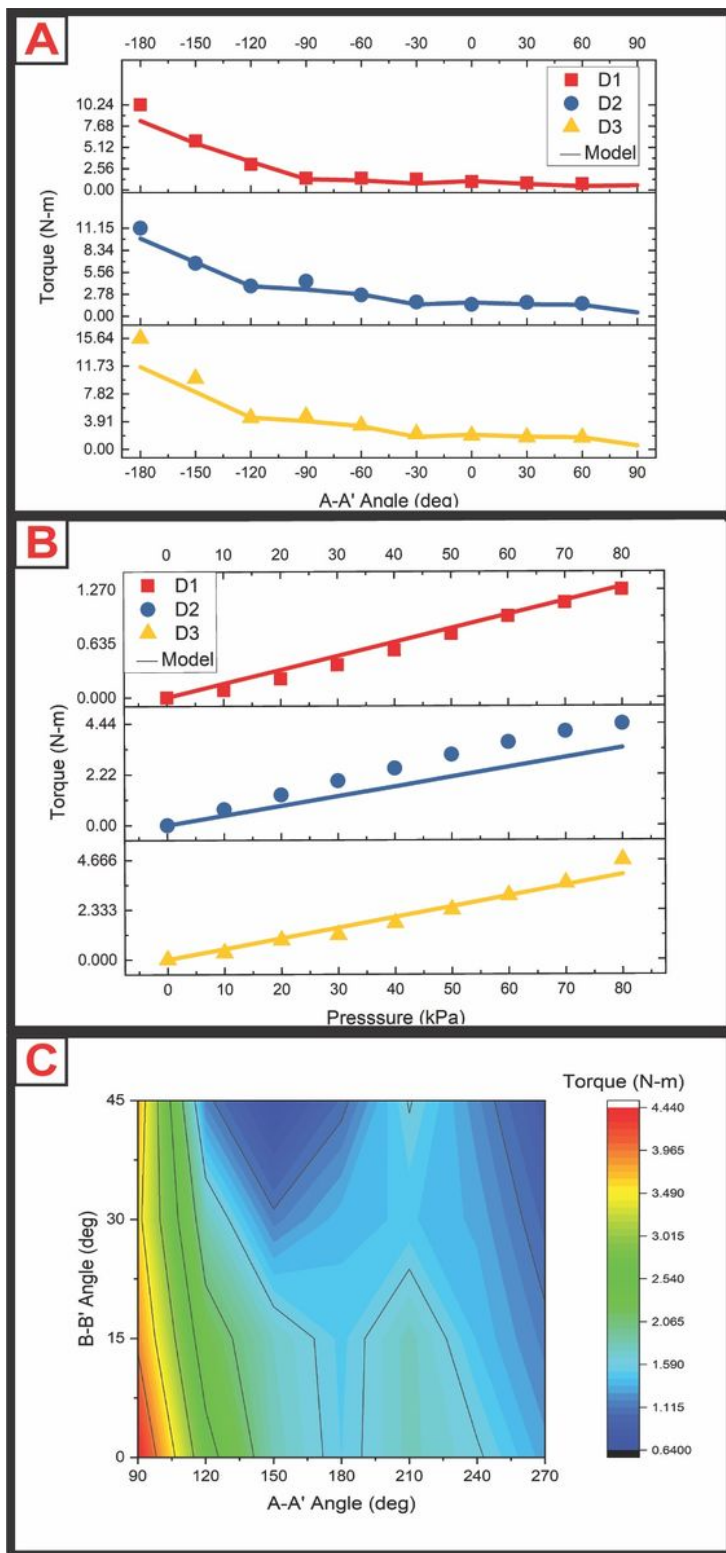


Figure 7

The experiment results for the actuator (A) Torque output as a function of A-A' angle when pressurized to 80kPa. (B) Torque output at various inflation pressures, at an A-A' angle set to 90°. Solid lines represent the output of the model. (C) A contour plot of torque output at various A-A' angles and B-B' angles for the D2 variant. (D) The waveform in response to a 60s square wave, with 0-80kPa peak-to-peak amplitudes. (E) The averaged step response during inflation. (F) The averaged step response during deflation.

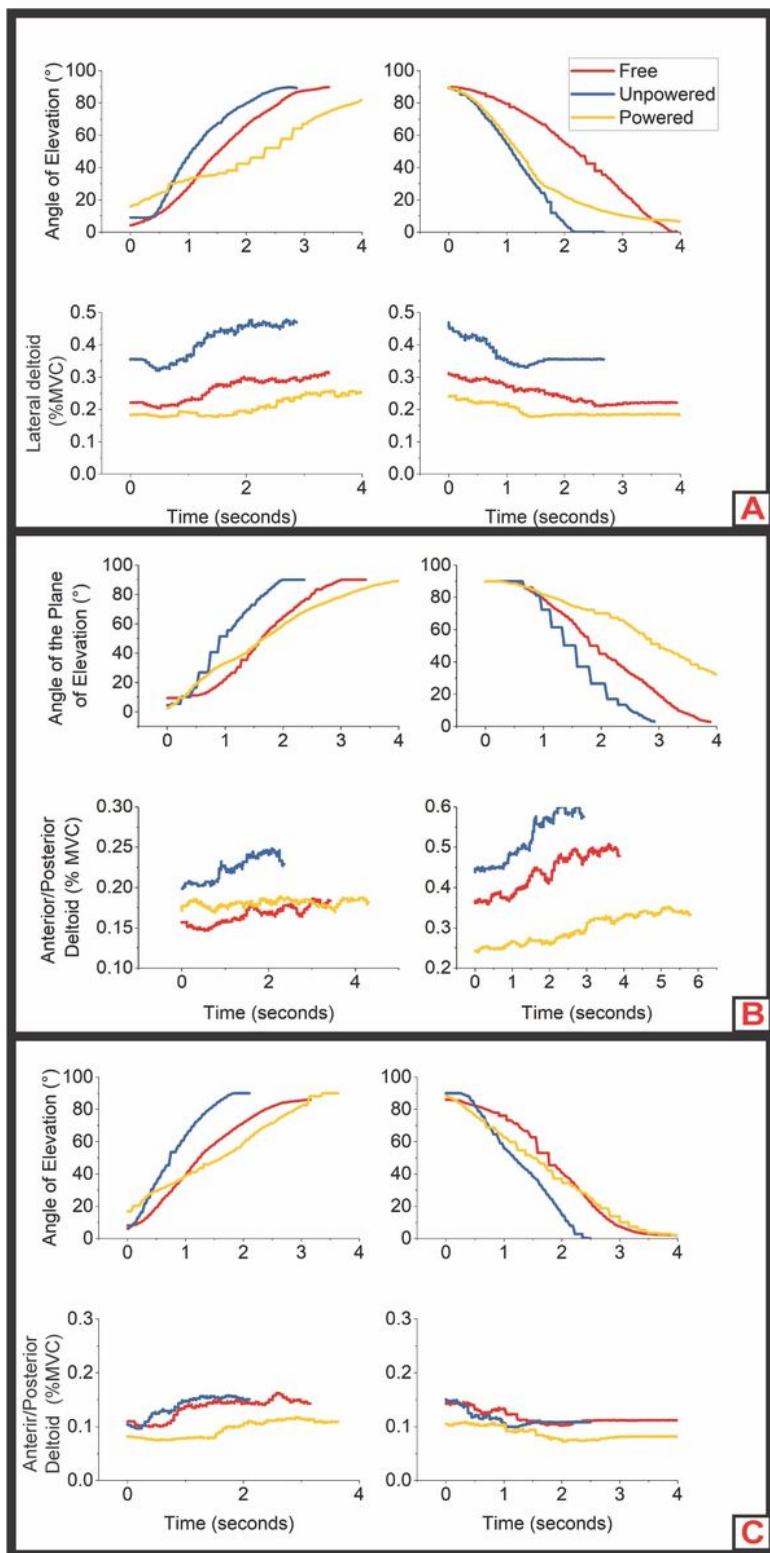


Figure 8

Segmented trajectory and muscle activation data sets extracted from a single subject. Representative muscles were chosen for visual illustration. (A) Abduction (Lateral Deltoid) and Adduction (Lateral Deltoid). (B) Horizontal Flexion (Anterior Deltoid) and Horizontal Extension (Posterior Deltoid). (C) Forward Flexion (Anterior Deltoid) and Forward Extension (Posterior Deltoid). Muscle activation

waveforms show a direct correlation with the corresponding trajectory. There is an apparent offset between free, unpowered and powered phases.

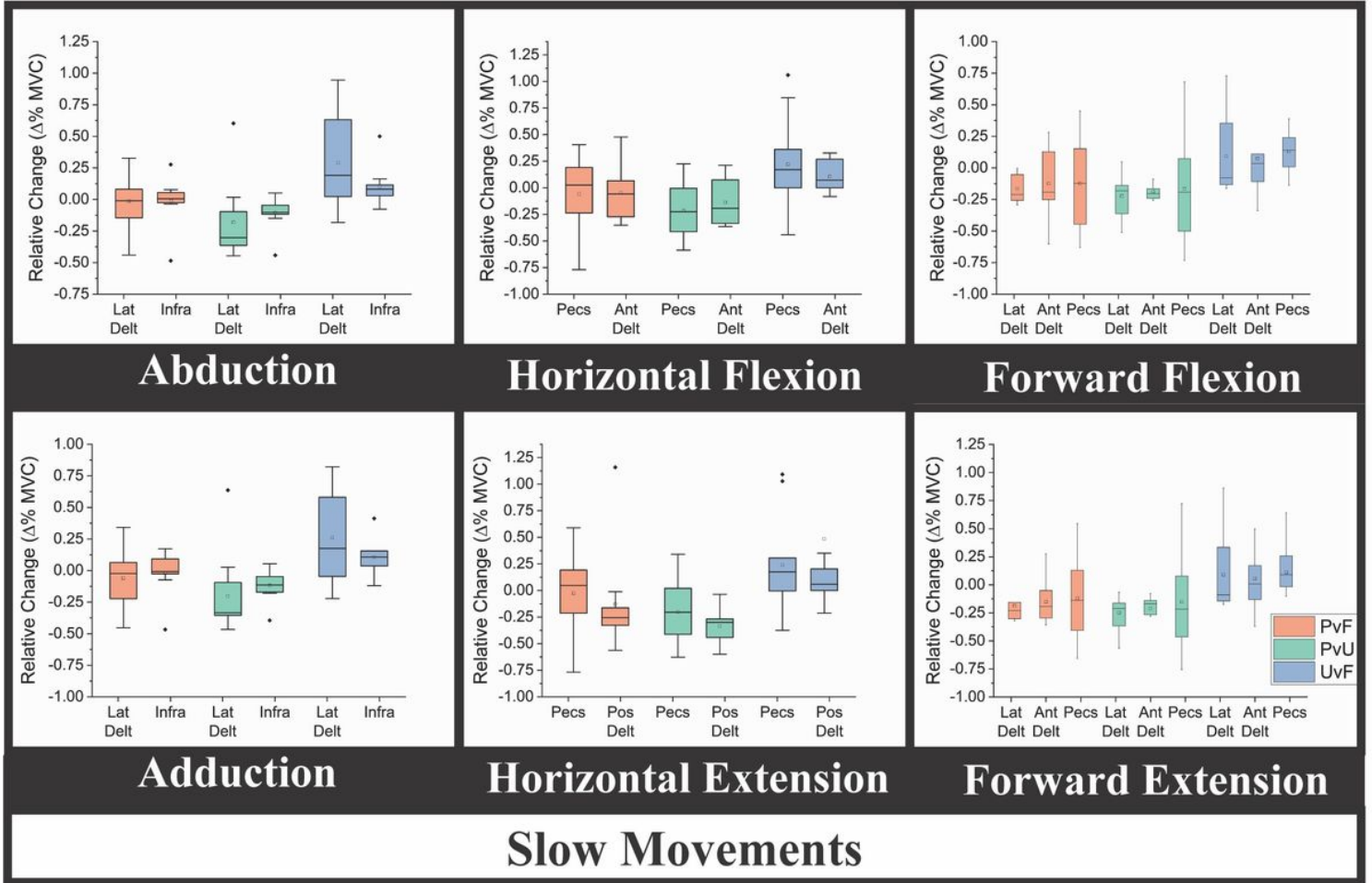


Figure 9

Box plots summarizing muscle activation data for slow movements. Lat Delt-Lateral Deltoid. Ant Delt-Anterior Deltoids. Pos Delt-Posterior Deltoid. Pecs-Pectoralis Major. Infra-Infraspinatus

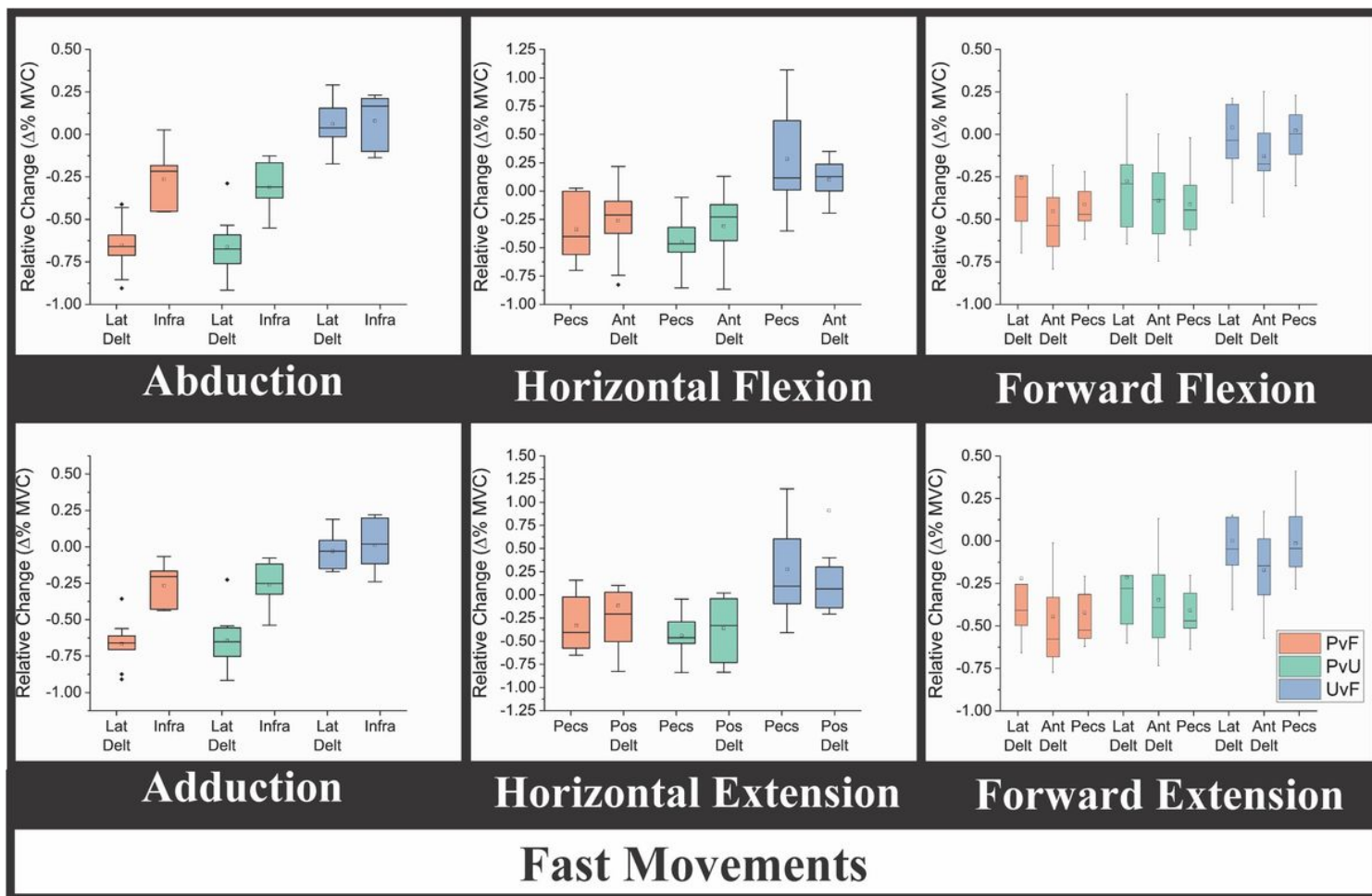


Figure 10

Box plots summarizing muscle activation data for fast movements. Lat Delt-Lateral Deltoid. Ant Delt-Anterior Deltoids. Pos Delt-Posterior Deltoid. Pecs-Pectoralis Major. Infra-Infraspinatus

Supplementary Files

This is a list of supplementary files associated with this preprint. Click to download.

- [AdditionalFile2.mp4](#)
- [AdditionalFile1R1.docx](#)